

# Adaptive Optics for Michelson Interferometry

## DIPLOMARBEIT

Ausgeführt zum Zwecke der Erlangung des akademischen Grades eines  
Diplom-Ingenieurs (Dipl.-Ing.)

unter der Leitung von  
Univ.-Prof. Dr.sc.techn. Georg SCHITTER  
Dipl.-Ing. Markus THIER

eingereicht an der  
Technischen Universität Wien  
Fakultät für Elektrotechnik und Informationstechnik  
Institut für Automatisierungs- und Regelungstechnik

von  
Georg Hoffmann, BSc.  
Matrikelnummer: 0625950  
Aribogasse 15/1/5  
1220 Wien, Österreich

Wien, im September 2014



---

## Abstract

---

Precise distance measurement is crucial for the high-precision industry as the semiconductor manufacturing is one. Measurement devices based on the concept of a Michelson interferometer are widely used to implement a very accurate and non-contact distance measurement with nanometer resolution. Interferometers are often applied in environments where the optical path is uncovered and influenceable by air turbulences such as caused by fast moving targets. Air turbulences cause aberrations in the wavefront, deteriorate the interference pattern and lead to a smaller peak-to-valley intensity signal which cause problems in the determination of the traveling distance.

To determine as well as to compensate for aberrated wavefronts this thesis investigates the integration of an adaptive optics system into a Michelson interferometer. The aberrated wavefront is measured with a Shack-Hartmann wavefront sensor and compensated by a deformable mirror. A feedback controller is implemented that computes the signals for the deformable mirror.

The proposed setup comprises off-the-shelf products for the interferometer and the adaptive optics setup. The implemented system is capable of compensating low order aberrations, resulting in an average improvement of 5, 7 of the peak-to-valley signal.



---

## Zusammenfassung

---

Die Verwendung von Interferometern zur exakten Distanzbestimmung ist vor allem in der Hoch-Präzisions-Industrie, wie etwa der Halbleiterfertigung, nicht mehr wegzudenken. Das berührungslose und nanometer-genaue Messprinzip auf Basis des Michelson Interferometers wird beispielsweise zur Positionierung von Waferstages bei deren Belichtung verwendet. Durch die steigenden Anforderungen bei immer höheren Taktraten auch entsprechend hohe Beschleunigungen zu erreichen, besteht die Gefahr von Luftverwirbelungen entlang des offenen Interferometer-Messpfades. Diese Luftverwirbelungen können dazu führen, dass durch unterschiedlich dichte Luft die ebene Wellenfront des verwendeten Lasers gestört wird. Da alle Aberrationen der Wellenfront im Messpfad bei der Interferenz mit dem Referenzpfad zu einem unerwünschten Interferenzmuster führen und dadurch die Signalstärke am Ausgang des Interferometers geschwächt wird, wird die exakte Positionierung erheblich erschwert.

Um diese Fehlerquelle einerseits zu bestimmen und andererseits auch zu kompensieren, wird in dieser Arbeit ein adaptives optisches System untersucht welches in ein Michelson Interferometer integriert wird. Die Aberration wird dabei mit einem Shack-Hartmann Wellenfront-Sensor gemessen und mittels eines deformierbaren Spiegels in einem Regelkreis kompensiert.

In dem vorgeschlagenen Aufbau werden jeweils für das Interferometer als auch für das adaptive optische System handelsübliche Komponenten verwendet was die Praxistauglichkeit und somit die einfache Integrierbarkeit in bestehende Systeme zeigen soll. Das realisierte System ist in der Lage Störungen niedriger Ordnung zu kompensieren und eine durchschnittliche Verbesserung des Ausgangssignal um den Faktor 5,7 konnte erreicht werden.



---

## Acknowledgment

---

Many people supported me during my academic studies. This page is here to say a big *thank you* to all of them and to show how grateful I am for the countenance and backup I received.

Firstly, a great thanks goes to my supervisors Univ.Prof. Dipl.-Ing. Dr.sc.techn. Georg Schitter and Dipl.-Ing. Markus Thier from Automation and Control Institute (ACIN) at the Vienna University of Technology for their expert knowledge, for sharing their scientific experience and of course for their personal mentoring. Without their great contribution this work would have never been possible. I also would like to mention the supporting and positive atmosphere at the laboratory carried from all the colleagues. Whenever I faced any problem or challenge somebody was here to listen, to advise or to encourage me.

The second great thank goes to my family and friends, especially my parents and my girlfriend Viktoria. Backing me up from all sides and enabling my academic studies is a great gift I'm obliged for. I particularly want to thank for encouraging me after every setback as well as celebrating all triumphs with me.





---

# Contents

---

<b>1</b>	<b>Introduction</b>	<b>1</b>
1.1	Motivation and Context . . . . .	1
1.2	Goal Definition and Challenges . . . . .	3
1.3	Approach . . . . .	3
1.4	Thesis Organization . . . . .	4
<b>2</b>	<b>Wavefront and Wavefront Aberrations</b>	<b>5</b>
2.1	Free Plane Wave . . . . .	5
2.2	Wavefront Aberrations . . . . .	6
2.3	Wavefront Reconstruction . . . . .	9
2.3.1	Zonal vs. Modal Reconstruction . . . . .	9
2.3.2	Zernike Polynomials . . . . .	9
2.4	Wavefront Error Metrics . . . . .	11
<b>3</b>	<b>Adaptive Optics System</b>	<b>13</b>
3.1	State of the Art . . . . .	14
3.1.1	Wavefront Sensor Technologies . . . . .	14
3.1.2	Deformable Mirror Technologies . . . . .	17
3.1.3	Conclusion . . . . .	18
3.2	Shack-Hartmann Wavefront Sensor . . . . .	19
3.2.1	Basic Working Principle . . . . .	19
3.2.2	Spot Detection . . . . .	20
3.2.3	Limitations . . . . .	21
3.2.4	Zernike Decomposition . . . . .	23
3.2.5	Implementation . . . . .	24
3.3	19-channel Piezo Deformable Mirror . . . . .	27
3.4	Feedback Control Algorithm . . . . .	28
3.5	Results 1: Control Capabilities . . . . .	30
3.5.1	Regularization Parameter . . . . .	31
3.5.2	Zernike Mode Forming Ability . . . . .	34

<b>4 Interferometer System</b>	<b>39</b>
4.1 Interferometer Principle . . . . .	39
4.2 Basic Michelson Interferometer . . . . .	42
4.2.1 Improvements for High-Precision Distance Measurement . . . . .	43
4.2.2 Disturbances in Interferometric Metrology . . . . .	46
4.2.3 Conclusion . . . . .	46
4.3 Experimental Setup . . . . .	47
4.4 Results 2: Evaluation of AO in the Interferometric Setup . . . . .	50
4.4.1 First Series of Tests: Influence of designated Zernike modes . . . . .	51
4.4.2 Second Series of Tests: Disturbance Compensation . . . . .	54
4.5 Conclusion . . . . .	57
<b>5 Outlook</b>	<b>59</b>
<b>Appendix A: Measurement Display</b>	<b>65</b>
1 Disturbances for Control Gain Finding . . . . .	65
2 Disturbances for Performance Testing . . . . .	67
<b>Appendix B: Setup Details</b>	<b>71</b>
3 Driving the Deformable Mirror . . . . .	71
<b>Appendix C: Software Functions</b>	<b>73</b>

---

## List of Figures

---

1.1	Photos of interference patterns . . . . .	2
2.1	Plane wave phase surface . . . . .	6
2.2	Point source sends spherical wave . . . . .	7
2.3	Aberration through refraction difference . . . . .	7
2.4	Spherical aberrations, Coma and Astigmatism . . . . .	8
2.5	First 21 Zernike modes . . . . .	10
3.1	Closed Loop AO setup . . . . .	14
3.2	LSI principle . . . . .	15
3.3	Pyramid wavefront sensor . . . . .	16
3.4	Segmented DMs . . . . .	17
3.5	Continuous-surface DMs . . . . .	18
3.6	SH schematic . . . . .	19
3.7	SH principle detail . . . . .	20
3.8	SH subaperture . . . . .	21
3.9	SH possible errors . . . . .	22
3.10	Used subaperture lenses . . . . .	25
3.11	SH spot patterns . . . . .	26
3.12	Photo of used DM . . . . .	28
3.13	Photo of AO setup . . . . .	30
3.14	Disturbance display . . . . .	31
3.15	Disturbance Zernike coefficients . . . . .	32
3.16	Comparison of $\beta$ . . . . .	32
3.17	L-curve . . . . .	33
3.18	Longrun RMS . . . . .	34
3.19	Voltage vector . . . . .	35
3.20	Astigmatism display . . . . .	36
3.21	Astigmatism Zernike coefficients . . . . .	36
3.22	Comparison of forming capability . . . . .	37
3.23	Purity of forming capability . . . . .	37

*List of Figures*

4.1	Two waves interfere . . . . .	41
4.2	Michelson interferometer schematic . . . . .	42
4.3	Direction of movement detection . . . . .	44
4.4	Use of PBS . . . . .	45
4.5	Schematic of used setup . . . . .	47
4.6	Photo of complete setup . . . . .	50
4.7	Drop of interference peak-to-peak value . . . . .	51
4.8	Comparison of interferometer's output signals . . . . .	52
4.9	Comparison peak-to-peak value for $c_{z3}$ . . . . .	53
4.10	[Comparison peak-to-peak value . . . . .	53
4.11	Disturbances RMS and PV . . . . .	54
4.12	Peak-to-peak value before and after compensation . . . . .	56
4.13	RMS after compensation . . . . .	56
1	Disturbance G1 . . . . .	65
2	Disturbance G2 . . . . .	65
3	Disturbance G3 . . . . .	66
4	Disturbance G4 . . . . .	66
5	Disturbance G5 . . . . .	66
6	Disturbance P1 . . . . .	67
7	Disturbance P2 . . . . .	67
8	Disturbance P3 . . . . .	67
9	Disturbance P4 . . . . .	68
10	Disturbance P5 . . . . .	68
11	Disturbance P6 . . . . .	68
12	Disturbance P7 . . . . .	68
13	Disturbance P8 . . . . .	69
14	Disturbance P9 . . . . .	69
15	Disturbance P10 . . . . .	69

---

## List of Tables

---

2.1	Zernike index translation . . . . .	10
2.2	Zernike denomination . . . . .	11
3.1	Commercially available SH sensors . . . . .	16
3.2	Initial RMS and PV . . . . .	33
4.1	Comparison before and after compensation . . . . .	57
1	Mapping DM indices . . . . .	71



---

## Acronyms

---

ACIN	Automation and Control Institute
ADC	analogue to digital converter
AO	adaptive optics
API	application programming interface
BW	black or white
CCD	charge coupled device
CoG	center of gravity
DAC	digital to analogue converter
DM	deformable mirror
FPGA	field programmable gate array
ILC	iterative learning control
LSI	lateral shearing interferometer
MMDM	micro-machined deformable mirror
OPL	optical path length
P-V	peak-to-valley
PBS	polarizing beam splitter
PC	personal computer
PMMA	polymethyl methacrylate, acrylic glass or Plexiglas®
RMS	root mean square
SH	Shack-Hartmann
SNR	signal to noise ratio
SVD	singular value decomposition
USB	universal serial bus





This chapter gives a brief introduction in which fields of application this thesis is located. The context of the topic and the motivation that drives this thesis is outlined together with the appearing of two concrete scientific questions that are investigated in the following. At last, the organization of this thesis is presented.

## 1.1 Motivation and Context

Laser interferometers are mainly used in the high-precision industry for positioning in the nanometer range. In a Michelson interferometer the interference of two coherent light waves, traveling through different optical paths, is evaluated. If one optical path is fixed as a reference and the other path is used for the measurement path, a change in the interference pattern can be interpreted as a distance change of the optical path. The amplitude of the acquired output signal heavily depends on the quality of the two interfering wave fronts and any disturbance, such as turbulent air in the laser beam of the interferometer's measurement path, would result in an aberration of the wavefront that decreases the output signal.

To correct wavefront aberrations, adaptive optics (AO) systems are commonly used. The performance and so the use of AO systems increased strongly in the last years. AO systems consist of a wavefront sensor like the popular Shack-Hartmann (SH) sensor, a deformable mirror (DM) and a feedback controller. Their ability to measure and compensate wavefront aberrations are used in many optical applications like astronomy, confocal microscopy, ophthalmology and others to increase image quality.

In this thesis an investigation is done on how an adaptive optics systems with a Shack-Hartmann wavefront sensor and a deformable mirror can counteract disturbances in an interferometer measurement path. For proving this idea, this thesis uses off-the-shelf products to show the applicability in a real measurement system.

## 1 Introduction

The propagation of light through an inhomogeneous medium causes an aberration of the wavefront. This happens because the wavefront of the propagating light travels through regions with locally different refraction indices which forces some parts of the wave to slow down more than others. The medium for example could be a gas (e.g. air) with fluctuating density because of temperature drift, an optical lens or anything with a nonuniform refraction index. To measure this kind of aberrations a wavefront sensor is used. Together with a DM, a device that can form its surface into certain shapes, and a feedback controller it is possible to actively compensate for wavefront aberrations. Such configurations are known as AO systems. AO systems are nowadays applied for example in astronomy where the atmosphere of the earth causes blurred images of the observed stars [1], in ophthalmology to compensate aberrations caused by the inhomogeneous human lens [2], and in optical communication systems to compensate signal degradation due to air turbulences [3].

Another field where wavefront aberrations distorts the measurement signal is interferometric metrology [4]. In the field of interferometry an interference pattern is created based on the phase relation of two overlaying beams.

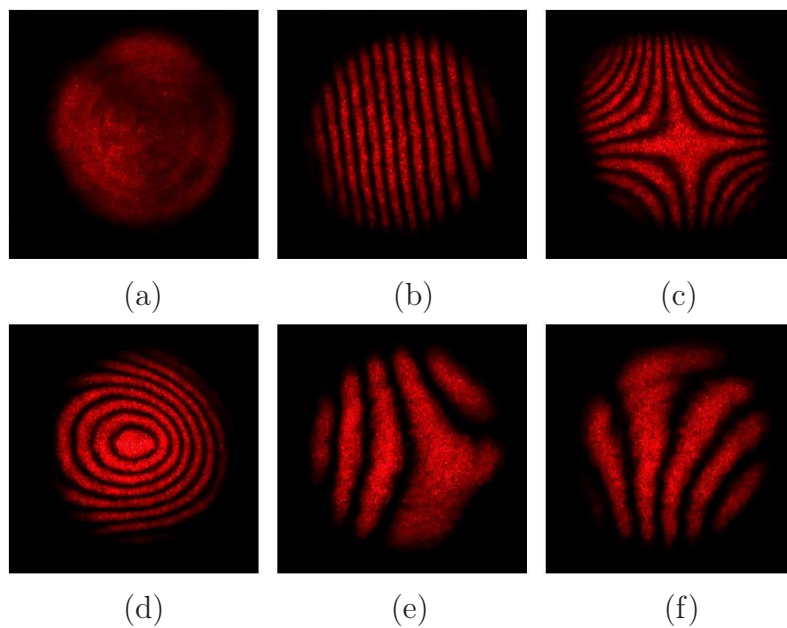


Figure 1.1: Photos of interference patterns. (a) shows the ideal case of a uniform pattern caused by non aberrated wavefronts. (b) - (f) show interference pattern caused by wavefront aberrations in the optical path of the measurement arm.

An often used instrument for performing relative distance measurements is the Michelson interferometer. In a Michelson interferometer the beam of a laser source is divided into two arms by a beam splitter, a reference arm and a measurement arm. The beams in both arms are reflected by mirrors and brought back together in the same beam splitter where they interfere. Depending on their phase difference they show constructive or destructive interference. In an ideal setup, constructive interference leads to a uniform bright intensity pattern at the detector whereas destructive

interference leads to a uniform dark intensity pattern. Due to wavefront aberrations in the optical path, e.g. caused by a tilt of the mirror in the measurement path or caused by air turbulences, a fringe pattern appears at the detector. In Fig. 1.1 a collage of different captured interference patterns is displayed showing distinct fringes as they would appear as interference pattern.

Usually, a lens focuses parts of the interference pattern onto a single photo-detector to measure the entire averaged intensity. A movement of the mirror in the measurement path causes the fringes of the interference pattern to wander. Every displacement of one half of a wavelength is equal to an inversion of the pattern which means that luminous fringes become dark and dark ones light up. The change in the intensity while moving is then proportional to the moved distance. The more fringes are inside the detection area, the less intensity variation is measured. Less intensity variation decreases the peak-to-peak signal range, hence reducing the signal to noise ratio (SNR) and so the achievable resolution. Thus, compensating for wavefront aberrations removes fringes from the intensity pattern and increases the SNR.

## 1.2 Goal Definition and Challenges

In this thesis an AO system is integrated into a Michelson interferometer. The implementation of an AO system in the measurement path of the interferometer is an attempt to increase the peak-to-peak signal range of the interferometer's output signal by counteracting any disturbances that would lead to an unwanted fringe pattern on the recording photo-detector. Doing so, the performance, robustness and availability of a Michelson interferometer should be enhanced. To accomplish this an investigation is needed on how wavefront aberrations influence the interferometer's output signal strength and how an AO system can counteract arbitrary disturbances in the interferometer's measurement path. From the described circumstances two specific questions arise that are investigated thoroughly in this thesis:

- *How are disturbances in the optical path of a Michelson interferometer affecting the output signal?*
- *Is an adaptive optics system capable to improve the peak-to-peak signal range of the interferometer's output if the measurement path suffers from disturbances?*

The focus in this thesis lies on a proof of concept if a particular improvement of a Michelson interferometer is achievable by using an AO system. Only static disturbances in the measurement path are considered and no special attention is paid to the controller speed.

## 1.3 Approach

At first, an adaptive optics system with a feedback controller is built which is capable to counteract wavefront aberrations. An iterative algorithm for the feedback controller is chosen. This AO system is then integrated into a Michelson interferometer whereby a homodyne laser is used as a light source and a half-silvered beam splitter is used

to divide the beam into the reference and the measurement path. A normal mirror reflects the beam in the reference part while a DM is used in the measurement path. To examine the influence of wavefront aberrations on the interferometer's output signal the DM of the AO system is used to generate distinct aberrations while the output is recorded. In a next step, disturbances are introduced into the measurement path and again the interferometer's output is measured but this time the AO system tries to compensate for the aberrations. All data is transferred to a personal computer (PC) where the computation and evaluation is done in MATLAB<sup>®</sup><sup>1</sup>.

The proposed approach in this thesis yields about a usage of commonly available items as they are already thoroughly tested, powerful, established on the market and therefore reasonably priced.

### 1.4 Thesis Organization

Chapter 2 introduces the term wavefront and wavefront aberration followed by a description of Zernike polynomials. The components of an AO system are described in Chapter 3 with special focus on the Shack-Hartmann wavefront sensor and the used piezoelectric driven deformable mirror. It follows the description of the feedback algorithm for closed loop control with corresponding implementation. Also the first part of the results is presented where the capability of the built AO setup is investigated. In Chapter 4 the interferometer setup is outlined, starting with an overview. A detailed view on the experimental setup used in this work and the results of the conducted experiments with the combined setup of AO and interferometer is also part of the chapter. Finally, future improvements and further investigations are discussed in Chapter 5.

---

<sup>1</sup>MATLAB<sup>®</sup> Version 2012b, The MathWorks<sup>®</sup> Inc., 3 Apple Hill Drive, Natick, Massachusetts

---

## Wavefront and Wavefront Aberrations

---

At first, the mathematical representation of an electromagnetic wave through the Maxwell's equations is presented followed by a description of wavefront aberrations. Secondly, the reconstruction of wavefronts by using Zernike Polynomials is presented together with wavefront error metrics.

### 2.1 Free Plane Wave

The basic description of an electromagnetic wave in free space is given by the homogeneous Maxwell's equations [5]. In a medium with constant permittivity  $\varepsilon$  and permeability  $\mu$ , as given in free space, the equations are as follows:

$$\vec{\nabla} \times \vec{E} + \mu \frac{\partial}{\partial t} \vec{H} = \vec{0}, \quad \vec{\nabla} \cdot \vec{E} = 0 \quad (2.1a)$$

$$\vec{\nabla} \times \vec{H} + \varepsilon \frac{\partial}{\partial t} \vec{E} = \vec{0}, \quad \vec{\nabla} \cdot \vec{H} = 0 \quad (2.1b)$$

Where  $\vec{E}$  is the electric and  $\vec{H}$  is the magnetic field strength. Introducing a phase function  $\theta(\vec{r}, t)$  for an electromagnetic field with  $\vec{E}(\theta)$  and  $\vec{H}(\theta)$  only depending on time and space whereby

$$\theta(\vec{r}, t) = ct - \vec{\kappa} \cdot \vec{r} \quad (2.2)$$

with constant speed  $c$  and a constant direction vector  $\vec{\kappa}$  (with  $|\vec{\kappa}| = 1$ ). One can see that surfaces with constant phase  $\theta$  are parallel to each other running with the same speed  $c$  as it is displayed in Fig. 2.1. The components in propagation direction of  $\vec{E}$  and  $\vec{H}$  are constant and so they are set to zero with no loss of generality:

$$\vec{\kappa} \cdot \vec{E} = 0, \quad \vec{\kappa} \cdot \vec{H} = 0 \quad (2.3)$$

As a conclusion, the free plane wave is transversal to its propagation direction.

It is now possible to eliminate either the electrical or the magnetic component from

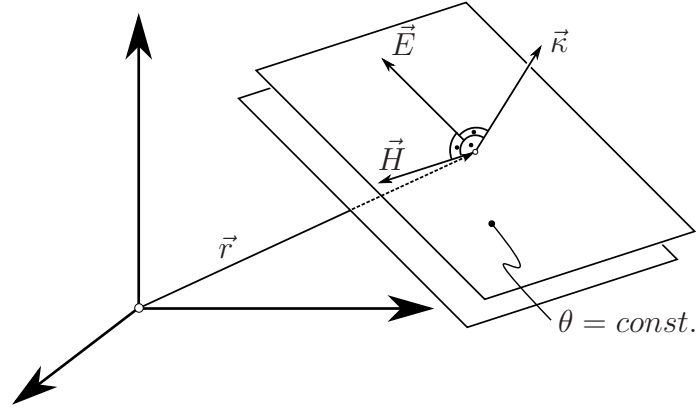


Figure 2.1: Phase surface of a plane wave traveling through free space (revised figure from [5]).

the homogeneous Maxwell's equation by expressing it through the other parameter. The formula for the electrical field is given by:

$$\left( \nabla^2 - \mu\varepsilon \frac{\partial^2}{\partial t^2} \right) \vec{E}(\vec{r}, t) = 0 \quad (2.4)$$

A solution of Eq. (2.4) is the flat sinus wave in an electrical non-conductive medium with constant  $\mu$  and  $\varepsilon$ :

$$\vec{E}(\theta) = \text{Re} \left[ \hat{\mathbf{E}}_0 e^{jk\theta} \right] \quad (2.5)$$

With the complex amplitude  $\hat{\mathbf{E}}_0$  and the propagation velocity  $c = \omega/k$  while  $\text{Re}[\ ]$  denotes the real part of the expression within the brackets.

Solving Eq. (2.1) and (2.2) for the Laplace operator in a spherical coordinate system results in wavefronts with spherical shape. Fig. 2.2 illustrates spherical wavefronts with corresponding rays emitted by a point source. The distance (in meters) between a  $360^\circ$  phase shift is called the wavelength  $\lambda$ . Furthermore, when considering a small portion of the spherical wavefront at a large distance, the spherical wavefront can be regarded as a plane wavefront.

## 2.2 Wavefront Aberrations

Wavefront Aberrations are describing any deviation of a light ray in respect to an ideal trace. This includes aberrations due to manufacturing failures in optical components, uneven distribution of the refraction index as well as any other disturbance that influences propagation of light rays in an unwanted way. A general description in form of a wavefront is provided in Fig. 2.3.

The plane wave is aberrated by the object with a refraction index  $n_2$  greater than the refraction index of the surrounding medium. It slows down the light partially and therefore the entire wavefront (i.e. connection of points with the same phase) is not flat any more. Light rays are indicated by the arrows as they stand perpendicular to the wavefront. Aberrations can be classified by the way on how they introduce deviation.

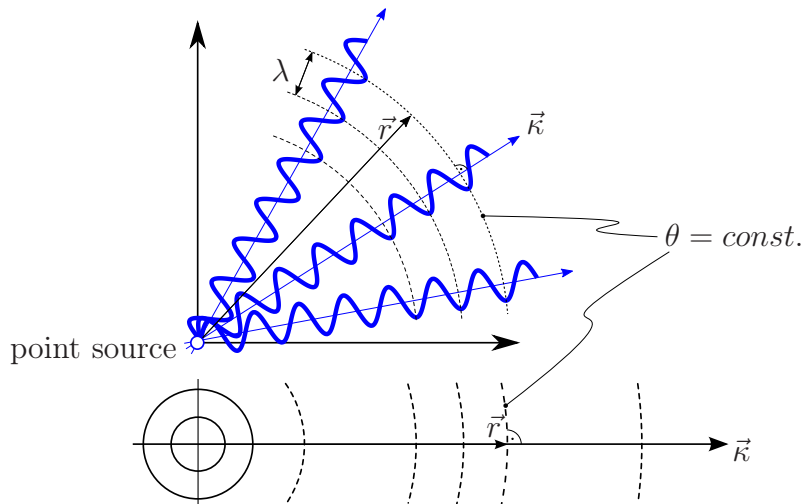


Figure 2.2: Point source sending out a spherical wave. Depicted are the distance from the origin  $\vec{r}$ , the wavelength  $\lambda$  and the propagation direction  $\vec{k}$ . Far away from the point source a small angular fraction looks like a plane wave. (revised figure from [6, p. 3])

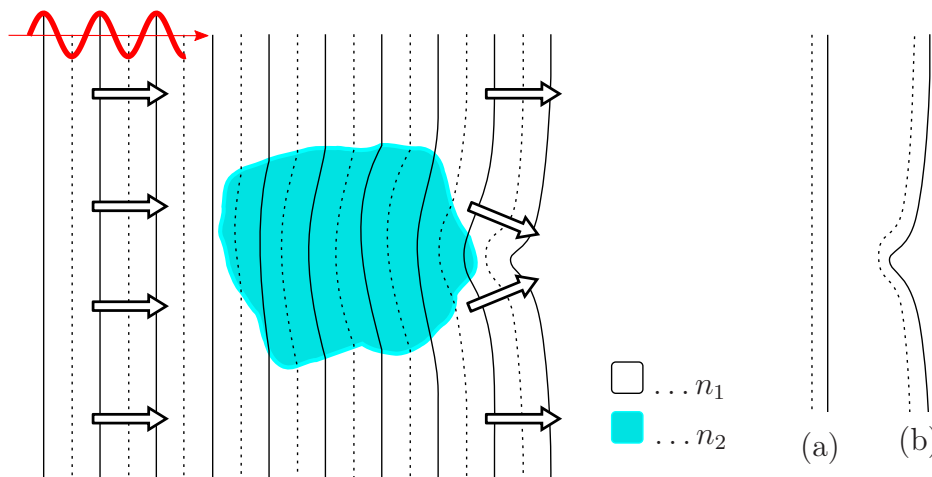


Figure 2.3: A plane wave, traveling from left to right, hits an object with a refraction index  $n_2 > n_1$ . Due to the slower propagation speed in the  $n_2$  medium, the flat wavefront get distorted. In (a) the ideal and in (b) the aberrated wavefront is depicted separately. (revised figure from [7, p. 471])

Three common aberrations for monochromatic light namely Spherical aberration, Coma and Astigmatism are shown in Fig. 2.4.

Ideal lenses are focusing all paraxial rays on the exact same spot at the nominal focal distance. The imperfection that paraxial rays are focused on different focal points, depending on their distance to the optical axis, is called *Spherical aberration* (see Fig 2.4a). The name is derived from the idea of using a sphere as a lens where this aberration would be at its maximum.

Similar applies to *Coma* (see Fig. 2.4b) where the incident rays are not paraxial but hitting the lens at a tilt. For an ideal lens the focal point would lie at the prolongation

of the center ray but lenses suffering from Coma are not able to form a sharp focus point in that case. Rays at the bottom are hitting the surface of the lens almost perpendicular while a sharp angle occurs on the top, leading to different deflection and a blurred focal point.

The last mentioned aberrations, the *Astigmatism* (see Fig. 2.4c), occurs if rays, propagating in two orthogonal planes, have different focal points. The orthogonal planes are often called tangential (or meridional) and sagittal plane. On one hand Astigmatism is observable if the curvatures of a lens is different in both mentioned planes. On the other hand it may also occur with symmetric lenses if the object is off the optical axis.

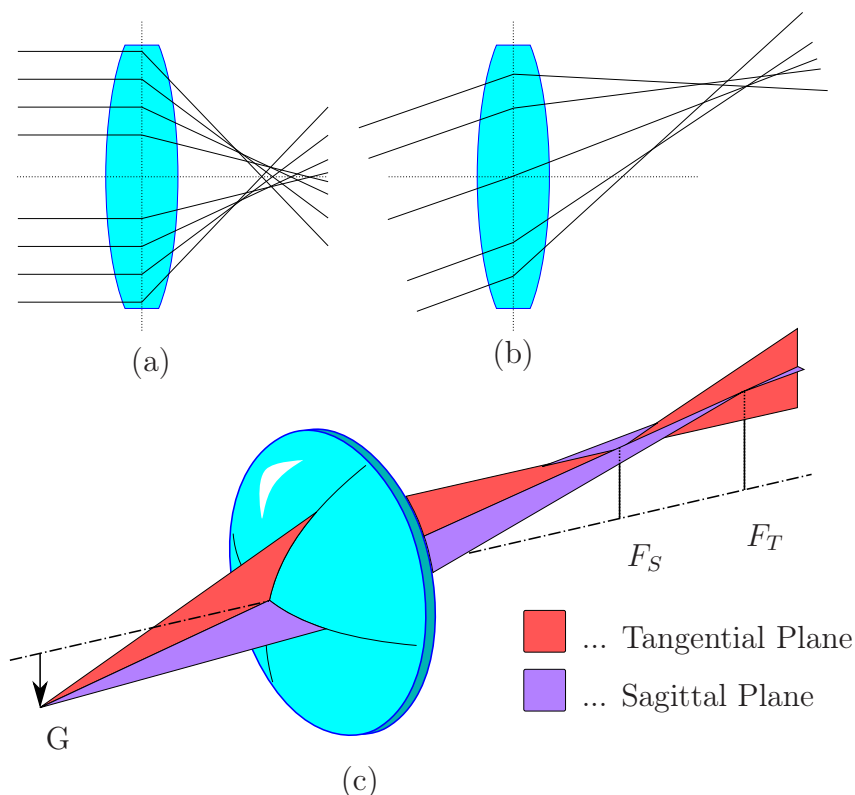


Figure 2.4: Spherical aberration in (a) shows different focal points of paraxial rays depending on the distance to the optical axis. In (b) Coma is displayed with non-paraxial rays focusing on different spots. The schematic in (c) shows the Astigmatism aberration for an object  $G$  positioned away from the optical axis and focusing on different spots for the tangential  $F_T$  and the sagittal plane  $F_S$  (schematic (c) is revised from<sup>1</sup>).

Beside deflection in the lens geometry, common sources of aberrations are density fluctuations and so fluctuations of the index of refraction in the optical path caused by e.g. air turbulences.

<sup>1</sup>Astigmatism Schematic, Author: *Michael Schmid*, under Creative Commons License



## 2.3 Wavefront Reconstruction

### 2.3.1 Zonal vs. Modal Reconstruction

To reconstruct any arbitrary wavefront into a three dimensional representation two approaches are presented. For the *zonal* approach the wavefront surface is divided by a rectangular grid and for every discrete node of the grid the local phase of the wavefront is derived from a linear equation that takes the runtime difference into account. The resulting set of linear equations can be written in matrix notation for further processing.

The *modal* approach reconstructs the wavefront from a set of basis functions. This polynomials are weighted with coefficients and super-positioned. A solution for the representation of a specific wavefront is found by determining the right coefficients. Since this approach is used widely in adaptive optics, mainly by employing the so called *Zernike Polynomials*, it is also used in this thesis.

### 2.3.2 Zernike Polynomials

Frits Zernike developed in the first third of the 20<sup>th</sup> century a method to describe wavefront aberrations and found a set of orthogonal polynomials defined inside a unit disc. They can be interpreted as the phase surface, i.e. the wavefront of a light beam. The so named Zernike polynomials are either even or odd and are defined as follows [8]:

$$Z_n^m(\rho, \varphi) = R_n^m(\rho) \cdot \cos(m\varphi) \quad (2.6)$$

$$Z_n^{-m}(\rho, \varphi) = R_n^m(\rho) \cdot \sin(m\varphi) \quad (2.7)$$

The function  $R_n^m(\rho)$  is called radial polynomial with the radius  $\rho$  and is defined as

$$R_n^m(\rho) = 0 \quad (2.8)$$

if the difference of  $(n - m)$  is odd. And in case  $(n - m)$  is even:

$$R_n^m(\rho) = \sum_{k=0}^{(n-m)/2} \frac{(-1)^k (n-k)!}{k! ((n+m)/2 - k)! ((n-m)/2 - k)!} \rho^{n-2k} \quad (2.9)$$

The positive integers  $m$  and  $n$  with  $n \geq m$  are the indices of the described Zernike modes. Since the radius  $\rho$  is only defined on the unity disk it's in a range between 0 and 1.  $\varphi$  describes the azimuthal angle of the function. The great advantage of this set of polynomials is that through their orthogonality any sufficiently smooth surface over the unity disk can be described by a composition of Zernike modes similar to a Fourier series for periodic functions. The requested surface  $W(\rho, \varphi)$  can be expressed by

$$W(\rho, \varphi) = \sum_{m,n} [a_{m,n} Z_n^m(\rho, \varphi) + b_{m,n} Z_n^{-m}(\rho, \varphi)] \quad (2.10)$$

with the coefficients  $a_{m,n}$  for the even and  $b_{m,n}$  for the odd part of the composition.

## 2 Wavefront and Wavefront Aberrations

An example of the first Zernike modes can be seen in Fig. 2.5.

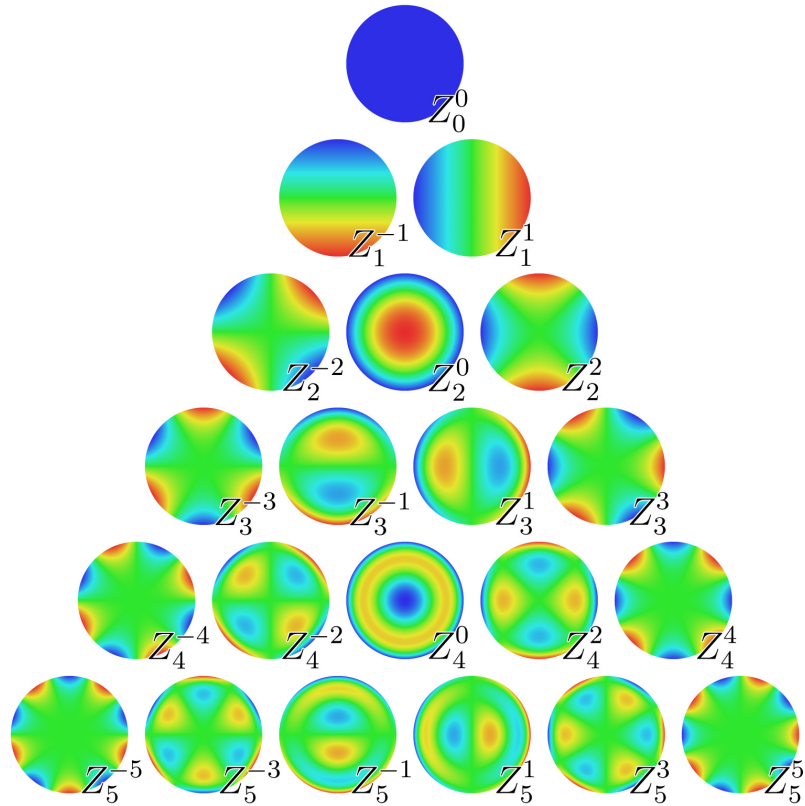


Figure 2.5: Depiction of the first 21 Zernike modes with their indices  $n$  and  $m$ .<sup>2</sup>

Sometimes it's handier to work only with one index  $j$  instead of two ( $m$  and  $n$ ). Therefore a translation between the two index notation and the one index notation is needed. One possible way is given by (see Table 2.1):

$$Z_n^m \rightarrow Z_j \quad \text{with} \quad j = \frac{n(n+2) + m}{2} \quad (2.11)$$

Table 2.1: Zernike mode indices translation.

m	0	-1	1	-2	0	2	-3	-1	1	3	-4	-2	0	2	4	-5	...
n	0	1	1	2	2	2	3	3	3	3	4	4	4	4	4	5	...
j	0	1	2	3	4	5	6	7	8	9	10	11	12	13	14	15	...

Often Zernike modes are not only called by their index but by their name. Common denominations are presented in Table 2.2 as they correspond to the description of aberrations in Chapter 2.2.

<sup>2</sup>Pictures of Zernike Modes, Author: *Rocchini*, licensed under Creative Commons License

Table 2.2: Zernike modes denomination.

j	denomination
0	Piston
1,2	Tilt
3,5	Astigmatism
4	Defocus
6, 9	Trefoil
7, 8	Coma
10, 14	Quadrafoil
11, 13	Secondary Astigmatism
12	Spherical Aberration

By using the single index  $j$  and the positions  $x$  and  $y$  instead of  $\rho$  and  $\varphi$  with

$$x = \rho \cos(\varphi) \quad (2.12)$$

$$y = \rho \sin(\varphi) \quad (2.13)$$

the description of an arbitrary wavefront  $W(\rho, \varphi)$  from Eq. (2.10) can also be expressed as:

$$W(x, y) = \sum_j c_j Z_j(x, y) \quad (2.14)$$

This formalism will be used further in this thesis since it provides a commonly used tool to describe wavefront aberrations.

## 2.4 Wavefront Error Metrics

To have a measure on how strong an aberration is compared to a flat wave one can perform a Zernike decomposition whereat the Zernike coefficients weigh the appearance of each Zernike mode. But sometimes it's more comfortable to express the aberration in terms of one single value. Therefore four different metrics for wavefront aberrations are presented:

- The *root mean square (RMS)* is calculated by applying the square root over the sum of the squared elements of the coefficient vector  $\mathbf{c}_Z = [c_{Z,1}, c_{Z,2}, \dots, c_{Z,n}]^T$ , utilizing the property of orthogonality of the Zernike polynomials [9].

$$RMS = \sqrt{\sum_{j=1}^n c_{Z,j}^2} \quad (2.15)$$

The root mean square (RMS) is often used to characterize disturbances or to evaluate the quality of a wavefront aberration compensation by the residual RMS. The unity of the RMS value is the unity of the coefficients but in most cases it is specified by orders of the used wavelength.

## 2 Wavefront and Wavefront Aberrations

- The *peak-to-valley* value is qualified to deliver an idea of the difference of the highest hill to the deepest valley of the measured wavefront. In contrast to the RMS it does not take the overall appearance into account but only uses the maximum and the minimum value.

$$PV = \max [W(x, y)] - \min [W(x, y)] \quad (2.16)$$

With  $W(x, y)$  representing the 3D representation of the captured wave. The unity is meter but similar to the RMS it is often specified by orders of the wavelength.

- *Purity* is used to express how strong a specific Zernike mode is present in an actual measurement [10]:

$$P_j = \frac{c_{Z,j}}{\sqrt{c_{Z,1}^2 + c_{Z,2}^2 + \dots + c_{Z,n}^2}} \quad (2.17)$$

The purity factor can take values in the interval between 0 and 1. This value is mainly used to investigate the Zernike mode forming capability of an DM. If for example the mirror is forced to form only one specific Zernike mode with the coefficient  $c_{Z,j}$  and the measurement with the SH sensor shows a coefficient vector  $\mathbf{c}_Z$  with non-zero elements aside to  $c_{Z,j}$ , the purity ends up in a value smaller than 1.

- The *Strehl Ratio* also plays an important role in imaging technologies to validate the quality of an optical system. It is defined as the ratio between the peak image intensity of a point source to the theoretically possible maximum intensity of a perfect system that is only limited by diffraction over the systems aperture.

$$S = \frac{1}{\pi^2} \left| \int_0^{2\pi} \int_0^1 e^{jW(\rho,\varphi)} \rho d\rho d\varphi \right| \quad (2.18)$$

The possible values are between 0 and 1 whereby an ideal system has the Strehl Ratio of 1.

---

### Adaptive Optics System

---

*"Adaptive Optics is a scientific and engineering discipline whereby the performance of an optical signal is improved by using information about the environment through which it passes." - [1, Page 1]*

To perform this kind of enhancement of an optical setup strategies were developed where a sensor determines the wavefront of the incident light and a deformable mirror counteracts wavefront disturbances by actively shaping its surface.

In Fig. 3.1 a basic layout of a closed loop AO setup is shown.

- The *original wavefront* coming from a light source (e.g. a laser) is depicted as a flat and coherent wave coming from the top. It goes through a
- *disturbance* e.g. an air turbulence (compare also Fig. 2.3). This leads to an uneven propagation of the incident light resulting in an
- *aberrated wavefront*. The wavefront surface is not flat any more.
- A *deformable mirror*, which is capable to form its surface complementary to the aberrated wavefront, reflects the light towards a
- *beam splitter* where one half of the intensity is forwarded to a
- *wavefront sensor* (e.g. a SH sensor). That sensor measures the residual wavefront and feeds the signal into the
- *controller* that drives the DM. Thus operates the system in a closed loop scheme such that the original wavefront (i.e. a flat wave) is recovered.
- A *science camera* on the second output of the beam splitter is used for further processing of the corrected wavefront signal. It can be seen as the output of the AO system where the disturbance is compensated.

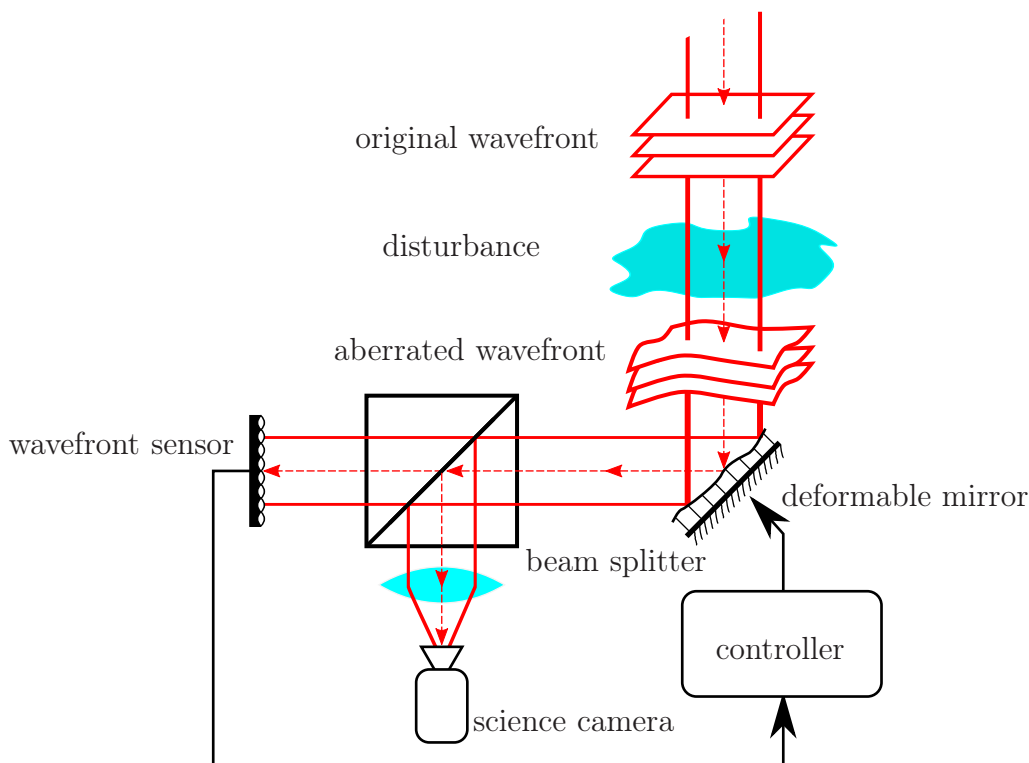


Figure 3.1: Functional schematic of a closed loop AO setup. The incoming wavefront is aberrated due to the disturbance and reflected off the DM which is actuated by the feedback controller accordingly to the signal from the wavefront sensor to compensate for aberrations. (revised figure from [11])

## 3.1 State of the Art

### 3.1.1 Wavefront Sensor Technologies

As described in the previous chapter the wavefront of a light beam is a connection of all points of a wave with the same phase ( $\theta = \text{const.}$ ). But since there is no detector available fast enough to measure the temporal frequency of light, an alternative method has to be found [12]. One conclusion of this is that light rays can be considered as constant or "frozen-in". So from the perspective of the frequency of light the difference between two rays is constant [6]. In other words if a wavefront is going through the same (constant) disturbance the output looks again constant. The other conclusion is that wavefront sensors are transforming the phase information (that can't be measured with electronics) into another domain like intensity.

In AO applications mainly two groups of sensors can be distinguished [1, p. 111]. The *indirect* approach actively influences the optical path by using a DM such that the phase of the wavefront is retrieved from the driving signals of the mirror. One example for an indirect method is a system where the phases of two beams are compared by letting them interfere on a detector [1, p. 153]. An active compensation device is fed by

the detectors signals and tries to maximize the intensity which is equivalent to a match of the phases of these two beams. Herein, the real wavefront is never calculated and involves some trial and error on how to feed back the signal which is time consuming and limited by the number of channels, thus not very common for good performing closed loop systems.

The *direct* approach measures the phase of an incident wave and reconstructs the wavefront out of this information. Direct methods are used more widely as they are more powerful thanks to modern computational power and additionally they provide a representation of the acquired wavefront. Three commonly used wavefront sensors that estimates the phase based on an intensity measurement are the lateral shearing interferometer (LSI), the Pyramid Sensor and the Shack-Hartmann (SH) sensor.

The LSI is based on the Mach-Zehnder interferometer although modern versions have different appearances. The incident beam is split into two components, whereat one component is shifted by the so called shearing distance  $\delta$ . The two beams are merged together to obtain interference fringes. These fringes represent the wavefront slopes in one direction which is equivalent to the derivative of the wavefront in this direction. For a two dimensional representation a second sensor perpendicular to the first one is needed to get also the derivation in the other spatial direction. The hardware setup for this wavefront measurement method is very complex depending on the number of utilized subapertures and according to [12] it was the most commonly-used interferometer before it was replaced by the Shack-Hartmann sensor.

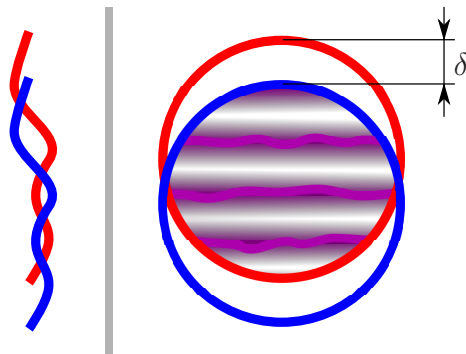


Figure 3.2: Schematic of the LSI principle with the sketched wavefronts on the left and the beams shifted by  $\delta$  on the right. The interference fringes in the overlapping zone represent the wavefront slope in shearing direction.

The Pyramid Wavefront Sensor uses a pyramidal prism with its top in the system focus to create four subbeams which are re-imaged onto a high-resolution detector via a relay lens [13]. The according schematic is drawn in Fig. 3.3. The difference of the intensity of the four resulting spots contains information about the x- and y- wavefront slopes which are the first derivatives of the incident wavefront. It is possible to use an array of pyramids in front of the same relay lens to form a layer oriented wavefront sensor. However, arrays of pyramidal prisms are not easily available at the moment. Another disadvantage is its increasing non-linearity at strong aberrations [14].

The Shack-Hartmann sensor consists of a microlens array in front of a detector. The detector is positioned in the focal distance of the microlenses so that an incoming flat wave results in an equally spaced pattern of focused spots, each in the middle

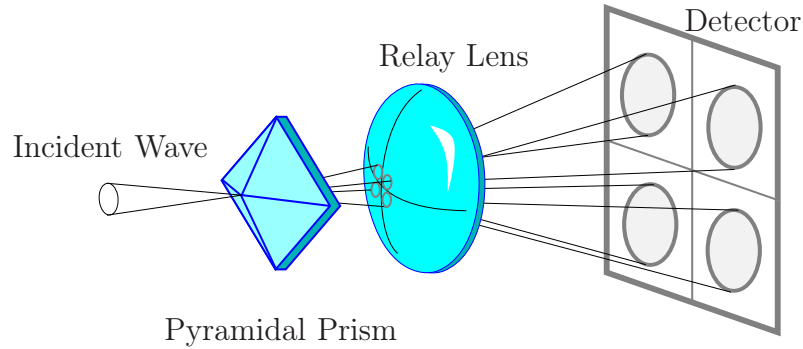


Figure 3.3: Schematic of a Pyramid Wavefront Sensor. An incident wave hits an pyramidal prism and creates four subbeams. The intensity difference of the four spots on the detector are proportional to the wavefront slope.

of their subaperture. If now a non-flat wave hits the sensor, every microlens would deliver a spot displaced from its optical axis according to the average wavefront tilt of this subaperture. The result is an image with uneven distributed spots, whereby every displacement of a spot, with respect to the reference position (e.g. the optical axis), delivers the spatial derivative of the captured wavefront. Table 3.1 shows technical parameters of commercially available Shack-Hartmann sensors that are typically used for research applications.

Table 3.1: Commercially available SH sensors, overview. All values are stated with their maximum as obtainable.

company & model	details	values
Imagine Optic SA <sup>1</sup> HASO <sup>TM</sup> 3 128-GE	frame rate:	7,5 fps
	lenses:	128 × 128
	aperture [mm <sup>2</sup> ]:	14,6 × 14,6
	accuracy:	$\lambda/100$
	connection:	GigaEthernet
OKO Technologies <sup>2</sup> UI-2210M, CCD	frame rate:	25 fps
	lenses:	20 × 20
	aperture [mm <sup>2</sup> ]:	4,5 × 4,5
	accuracy:	$\lambda/150$
	connection:	USB 2.0
Thorlabs GmbH <sup>3</sup> WFS10-7AR 180 × 180 px	frame rate:	450 Hz
	lenses:	41 × 29
	aperture [mm <sup>2</sup> ]:	6,34 × 4,76
	accuracy:	$\lambda/10$
	connection:	USB 2.0

<sup>1</sup>Imagine Optic SA, 18 rue Charles de Gaulle, Orsay 91400, France

<sup>2</sup>Flexible Optical B.V., Polakweg 10-11, 2288 GG Rijswijk, the Netherlands

<sup>3</sup>Thorlabs GmbH, Hans-Boeckler-Str. 6, Dachau/Munich 85221, Germany



### 3.1.2 Deformable Mirror Technologies

Deformable Mirrors are devices with the ability to actively shape their surface. They can be distinguished in terms of size, number and working principles of actuators, achievable stroke and speed. While for astronomical applications the diameter of the active surface can go up to several meters and the number of actuators is a few thousands such as used for the European Extremely Large Telescope, E-ELT [15] in other fields like ophthalmology the size is considerably smaller, namely in the range of centimeters and the number of actuators is between 10 to 100 [16]. In the beginning of DMs the surface was segmented and each segment was actuated separately. The principle was to apply only a piston like movement per segment, as depicted in Fig. 3.4a. Advanced versions added a tilt functionality carried out by two actuators per segment, as seen in Fig. 3.4b.

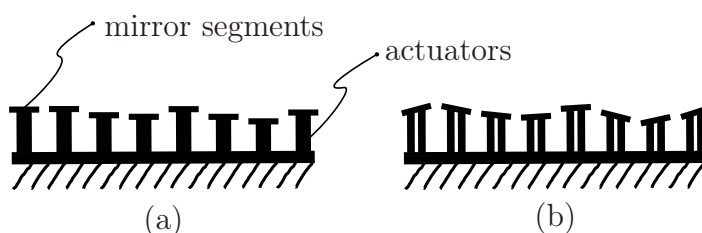


Figure 3.4: (a) shows the segmented mirror with piston displacement and (b) displays the segmented mirror with tilt functionality.

With the enhanced possibilities in manufacturing micro machined structures it was possible to produce DMs with a continuous-surface, as shown in Fig. 3.5a. They don't suffer from scattered light from the edges of the segments, have no loss of light in the gaps between segments and are able to form a completely smooth surface. Different actuator techniques are utilized to bend the surface as for example voice coils, piezo stacks or even worm gears.

The piezo driven DM as shown in Fig 3.5a, has a certain number of distinct piezo stacks with a plate-like mirror bonded on top of them [17]. The actuators of the mirror are driven by a relatively high (several hundreds volts) positive or negative voltage, thus it is able to push or pull the surface. The rim of the plate is not fixed and can move freely, such that the mirror can also perform piston movements. The arrangement of the piezo stack layout is an important characteristic of a device and varies for different applications because every actuation of one stack causes global deformation of the plate and effects also the neighboring actuators.

A different approach is provided by membrane mirrors, also called micro-machined deformable mirror (MMDM) [18]. The MMDM is basically a membrane with fixed edges and an array of electrodes beneath it. They are manufactured with the technology of bulk micro-machining and therefore they are comparably cheap to other technologies. If a voltages is applied between the membrane and one (or multiple) of the electrodes the electrostatic attraction bends the membrane into the desired shape. Applying a constant potential to all electrodes forces the mirror into a concave shape and by biasing the electrodes the mirror is able to work in both directions by releasing or increasing electrostatic force. They are commercially available in sizes from about half

### 3 Adaptive Optics System

a centimeter up to 50 mm in diameter and a thickness of the membrane from 0,5 to 10  $\mu\text{m}$ . The schematic is displayed in Fig. 3.5b.

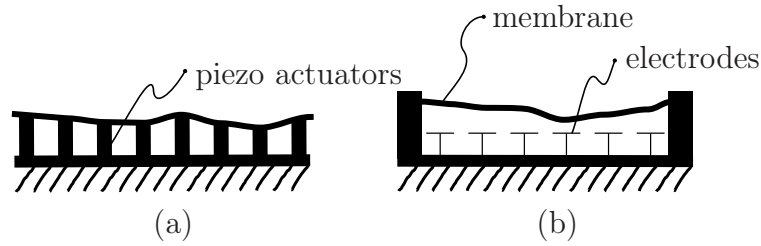


Figure 3.5: Two mirrors with a continuous-surface. In (a) a piezo driven mirror with a free edge is shown while in (b) a membrane mirror with a fixed rim is displayed. The second one is driven by electrostatic forces applied by the marked electrodes.

In [10] an improvement to the electrostatic MMDM technique is presented which introduces push-pull capability to increase the performance. It is achieved mainly with transparent electrodes out of indium-tin-oxide coated glass at the mirrors top surface. They work the same way as the bottom electrodes by applying electrostatic force to the membrane.

The piezo driven DM and the MMDM, both with a continuous surface, are the most common mirrors used for adaptive optics. A comparison of DMs with different actuation principles is done in [19]. They show that on one hand the higher stroke of a piezo-actuated mirror gives a vital advantage compared to a MMDM but on the other hand the measured hysteresis of the piezo-actuated mirror was about 14% of its maximum stroke. Furthermore, hysteresis necessitates an approach with an adequate feedback control.

#### 3.1.3 Conclusion

Shack-Hartmann wavefront sensors are well established, commonly used, robust and universally usable devices to capture arbitrary wavefront aberrations, so this principle is used in this thesis as wavefront sensor. They are able to capture an incident wavefront with a single shot and the quality of the measurement depends on the number of microlenses as well as the correct detection of the center of the focused spots. In this thesis, the OKO Technologies SH sensor (from Table 3.1) is used, which provides a good accuracy however a moderate frame rate that is sufficient since only quasi-static aberrations are compensated.

Due to its advantage in providing a higher stroke a piezo-actuated DM is used as the active part in the AO system. A model with 19-channels is used with a maximum stroke of 8  $\mu\text{m}$  at 400 V and it's provided by the same manufacturer as the SH sensor, OKO Technologies. Due to the mentioned issue of strong hysteresis of piezo stacks, the mirror is driven in a feedback setting with the captured wavefront from the SH sensor as input for the feedback control.

## 3.2 Shack-Hartmann Wavefront Sensor

The used Shack-Hartmann sensor is a device from OKO Technologies with a  $20 \times 20$  lens array in front of a  $640 \times 480$  pixels CCD USB camera. The following section gives an detailed overview on how the SH sensor principle works and how the incident wave can be recovered. Followed by an introduction on how wavefront surfaces can be represented by Zernike polynomials.

### 3.2.1 Basic Working Principle

The SH sensor comprises of two main components, an image sensor such as a CCD and a microlens array. The microlens array is mounted at its focal distance in front of the image sensor. The sensor area is divided into so called subaperture, whereby every microlens focuses into one of them. The schematic of the sensor is shown in Fig. 3.6. In case of a plane wave as shown in Fig. 3.6a, the incoming light wave is segmented and focused to small spots on the detector, forming a pattern of equally distributed spots. The spots are exactly in the middle of each subaperture. In the case of an aberrated wavefront, each lens doesn't focus on its optical axis anymore, as depicted in Fig. 3.6b.

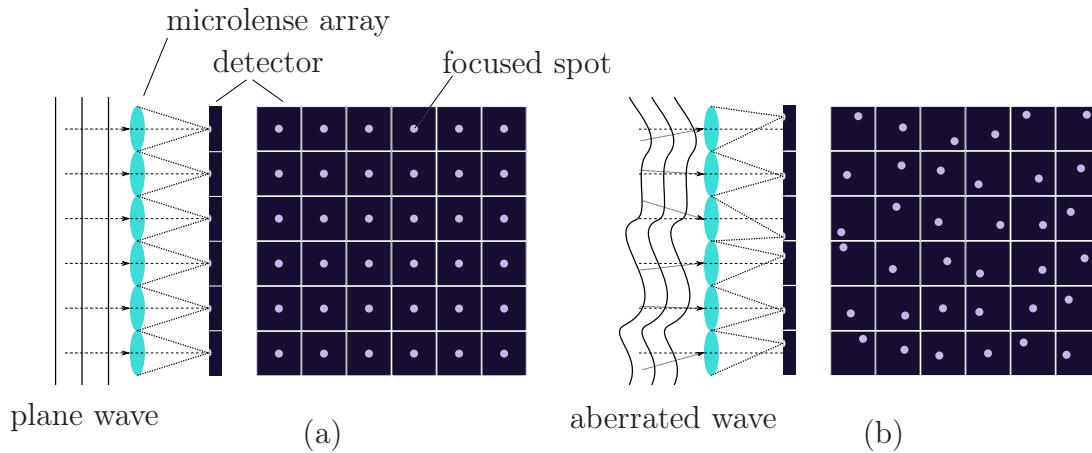


Figure 3.6: A light wave hits the microlens array of a SH sensor and generates a pattern of focused spots on the detector. In (a) the plane wave leads to equally spaced dots while in (b) an aberrated wave leads to an uneven pattern.

The resulting spot of each corresponding lens shows a displacement to the optical axis, originating from the average wavefront tilt, as depicted in Fig. 3.7. The relation between wavefront slope (tilt) and spot displacement is given by [9]:

$$\frac{\Delta x}{f} = \frac{\partial W(x, y)}{\partial x} = s_x \quad (3.1)$$

$$\frac{\Delta y}{f} = \frac{\partial W(x, y)}{\partial y} = s_y \quad (3.2)$$

Where  $s_x$  and  $s_y$  are the slopes in x and y direction and  $\Delta x$  and  $\Delta y$  denote the spot displacement. By using a reconstruction algorithm the wavefront slopes are transformed

into a continuously modeled wavefront.

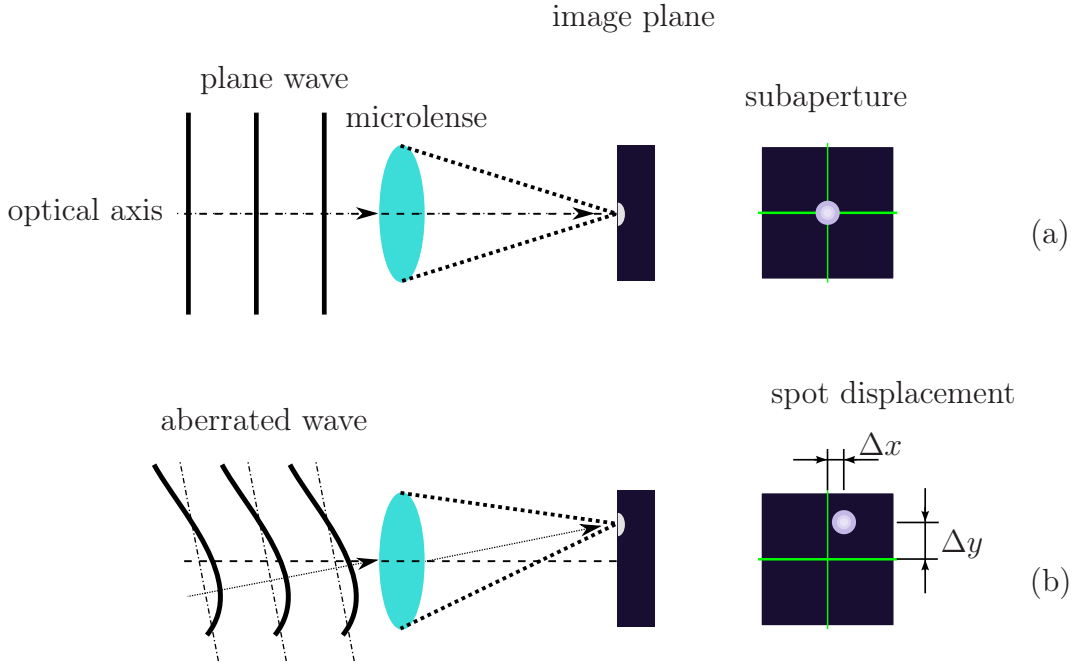


Figure 3.7: This depiction is a detail of Fig. 3.6. The incoming wavefront generates a spot on the detector depending on its average tilt. As seen in (a) an incoming plane wave produces a spot in elongation of the optical axis while in the aberrated case (b) the spot is shifted from the center position by  $\Delta x$  and  $\Delta y$ .

### 3.2.2 Spot Detection

One challenge in the SH principle is to locate the exact position of the spots within one corresponding subaperture of the sensor. It has to be noted that the focused spots are not points of the size of one pixel but are disks of several pixels. Therefore a method is needed to find the centroids of the spots. The most frequently used algorithm is the center of gravity (CoG) calculation where the discrete intensity values are multiplied by the position of the pixels, summed up and divided by the overall intensity:

$$CoG_x = \frac{\sum_{x=1}^n \sum_{y=1}^m x \cdot I(x, y)}{\sum_{x=1}^n \sum_{y=1}^m I(x, y)} \quad CoG_y = \frac{\sum_{x=1}^n \sum_{y=1}^m y \cdot I(x, y)}{\sum_{x=1}^n \sum_{y=1}^m I(x, y)} \quad (3.3)$$

The variables  $x$  and  $y$  are integer values of the  $n \times m$  subaperture and the subaperture size was determined to  $19 \times 19$  pixels. As seen in Fig. 3.8 the coordinates of the center of gravity (CoG) ( $CoG_x$  and  $CoG_y$ ) are not necessarily integer values but floating-point numbers. The value of the intensity of each pixel, stated as  $I(x, y)$ , depends on the bit resolution of the image sensor, which is 0 to 255 for the SH sensor used in this thesis.

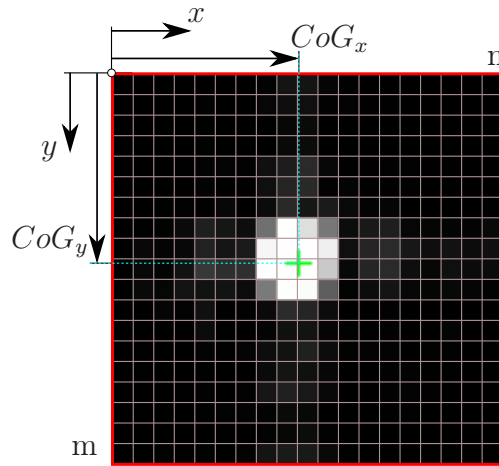


Figure 3.8: Picture of a subaperture of  $19 \times 19$  pixels size. The intensity value of each pixel is used to find the center of the spot via the CoG algorithm from Eq. (3.3).

Different methods to gain accuracy in the centroid calculation by reducing the influence of present noise are reported. Some of them aiming on the improvement of the presented basic CoG algorithm shown in Eq. (3.3) like the *Thresholding CoG* (TCoG) or the *Weighted CoG* (WCoG). The TCoG method basically subtracts a threshold from the intensity values which can reduce detector noise while the WCoG weights the intensity value of each pixel with a function depending on its position [20]. For the implementation of the WCoG method further information of the expected region of the spot is necessary such that noisy pixels in the outer region of the subaperture can be suppressed. Other techniques utilize *Correlation Algorithms* where a template of an ideal prototype spot is cross-correlated with the examined subaperture [20]. The centroid is then retrieved from the best matching of the ideal spot with the subaperture.

As the proposed setup is capable of adjusting the incident laser intensity onto the SH sensor, the settings of the image sensor are tuned in a way that noise is negligible. Therefore the basic CoG formula from Eq. (3.3) works well and sufficient for the presented implementation. Since the SH sensor will be used in a closed loop arrangement absolute exact measurements are not necessary because the controller takes care of any residual deviation. Furthermore it will be expected that the residual error caused by the limited mirror shape due to the finite number of createable mirror modes is far more significant than the difference between the diverse CoG algorithms, especially when a good contrast of the spots can be achieved. When thinking about high speed implementation the simple CoG is also advantageous in terms of processing effort and time.

### 3.2.3 Limitations

One major issue of a SH sensor is its time consuming read out. Every time a wavefront is captured a full resolution picture is processed to get the information about the

wavefront. A deeper investigation is done in [21] where also a field programmable gate array (FPGA) implementation of a fast wavefront reconstruction is presented. Another drawback of the SH sensor is that there are wavefronts that lead to a corrupted or false interpretation. As depicted in Fig. 3.9, three main erroneous cases can be distinguished. The first case appears when the incident wave has such a tilt that the corresponding spot lies in the next subaperture. Multiple spots in one subaperture are not evaluable since it can't be determined which spot is coming from which lens. With the help of an intelligent algorithm, that is used to evaluate the position of the spots, at least the occurrence of an error can be detected. Obvious in the second case is that if no spot is detected in a subaperture no interpretation is legit. And thirdly a crossover of two spots appear when the incoming wavefront is curved in a way that two lenslets are pointing in each others subaperture. The problem in this case is that the spot finding algorithm is not able to detect any error but the computed wavefront is not the real one. Since these problems occur only at highly aberrated waves it is not very relevant in a closed loop setup because the residual error is kept as small as possible.

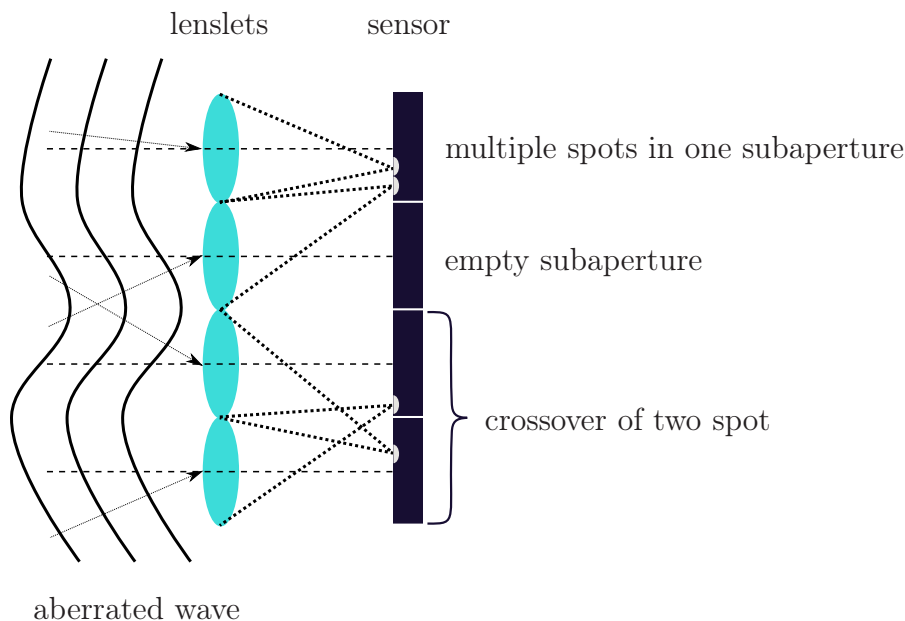


Figure 3.9: A strongly aberrated wave hits the microlens array and leads to different kind of errors. Multiple spots in the first subaperture, no spot in the second and a crossover in the third and fourth. (revised figure from [2, p. 71])

One further limitation of a SH sensor is that a phase difference of the entire wavefront, also known as piston mode, can not be detected. If all points of the wave are suffering from the same phase delay it is not possible to detect it since the lenslets would still focus on the same spots.

### 3.2.4 Zernike Decomposition

The decomposition of any measured disturbance into the coefficients of the Zernike modes is done by using the slopes  $\mathbf{s}_x$  and  $\mathbf{s}_y$ . This slopes are the displacements of the spots for every single subaperture  $k$  divided by the focal length  $f$  of the micro-lenses:

$$s_{kx} = \frac{CoG_{kx} - CoG_{kx,ref}}{f} \quad (3.4)$$

$$s_{ky} = \frac{CoG_{ky} - CoG_{ky,ref}}{f} \quad (3.5)$$

$CoG_x$  and  $CoG_y$  are calculated by Eq. (3.3) and represent the current spot position.  $CoG_{x,ref}$  and  $CoG_{y,ref}$  are positions from a reference spot obtained either by taking a reference wavefront (e.g. a captured wavefront of the optical setup without any disturbance) or by using the imaginary center of the subaperture. To collect the  $x$  and  $y$  direction into one vector the slope vector can be written as

$$\mathbf{s}_{xy} = \mathbf{s} = [s_{x1}, s_{y1}, s_{x2}, s_{y2}, \dots, s_{xn}, s_{yn}]^T. \quad (3.6)$$

The relation between the slopes and the wavefront expressed in terms of Zernike polynomials is [2]:

$$\mathbf{s} = \mathbf{Z}\mathbf{c}_z \quad (3.7)$$

Where the vector  $\mathbf{c}_z$  contains the coefficients of the Zernike modes and the matrix  $\mathbf{Z}$  is called the reconstruction matrix comprising of the first derivative of the Zernike polynomials:

$$\mathbf{Z} = \begin{pmatrix} \mathbf{Z}_{11x} & \cdots & \mathbf{Z}_{1jx} & \cdots & \mathbf{Z}_{1Jx} \\ \mathbf{Z}_{11y} & \cdots & \mathbf{Z}_{1jy} & \cdots & \mathbf{Z}_{1Jy} \\ \vdots & \ddots & \vdots & \ddots & \vdots \\ \mathbf{Z}_{k1x} & \cdots & \mathbf{Z}_{kjx} & \cdots & \mathbf{Z}_{kJx} \\ \mathbf{Z}_{k1y} & \cdots & \mathbf{Z}_{kjy} & \cdots & \mathbf{Z}_{kJy} \\ \vdots & \ddots & \vdots & \ddots & \vdots \\ \mathbf{Z}_{K1x} & \cdots & \mathbf{Z}_{Kjx} & \cdots & \mathbf{Z}_{KJx} \\ \mathbf{Z}_{K1y} & \cdots & \mathbf{Z}_{Kjy} & \cdots & \mathbf{Z}_{KJy} \end{pmatrix} \quad (3.8)$$

Whereby:

$$\mathbf{Z}_{kjx} = \frac{\iint_k \frac{\partial Z_j(x,y)}{\partial x}}{\iint_k dx dy} \quad (3.9)$$

$$\mathbf{Z}_{kjy} = \frac{\iint_k \frac{\partial Z_j(x,y)}{\partial y}}{\iint_k dx dy} \quad (3.10)$$

The index  $j$ , running from 1 to  $J$ , names the Zernike modes in ascending order whereby  $Z_J$  represents the highest utilized mode and the index  $k$  numbers the subapertures of the wavefront sensor (as shown in Fig. 3.10 in Chapter 3.2.5) running from 1 to  $K$ .

### 3 Adaptive Optics System

Since the values for the reconstruction matrix are discretized for each subaperture ( $k = 1 \dots K$ ) the question is raised either to use the average value or the value of the Zernike gradient at the center of each subaperture. For practical usage, calculating the Zernike gradient at the center of the subaperture is sufficient.

Consequential two values are still open to be defined as the first is the maximum number of Zernike modes  $J$  that are used for the decomposition and the other is the number of used subapertures  $K$ . For the current implementation of the decomposition a value of  $J = 20$  is chosen because (i) of a decent balance between computational cost and proper reconstruction and (ii) the DM is only able to create shapes up to mode 15 as seen in the Results in Chapter 4.4. For a precise reconstruction of a certain mode (the higher the mode number, the higher is the spatial frequency), large spatial oversampling of the wavefront is needed, meaning that the ratio of the number of subaperture to the mode number has to be large. The number of used lenslets  $K$  is basically derived from the available beam diameter. If the intensity of the laser beam is not distributed evenly over the beam diameter (e.g. brighter center), then it could be necessary to exclude the outer spots because they may introduce an inaccurate reconstruction due to noise.

For the wavefront reconstruction the slopes are measured by the wavefront sensor and Eq. (3.7) is inverted, yielding the following formalism:

$$\mathbf{c}_z = \mathbf{Z}^\dagger \mathbf{s} \quad (3.11)$$

With  $\mathbf{s}$  as slope vector,  $\mathbf{Z}^\dagger$  as pseudo-inverse of the reconstruction matrix and  $\mathbf{c}_z$  as the coefficient vector for the Zernike polynomials. Since  $\mathbf{Z}$  is not quadratic, an algorithm such as the singular value decomposition (SVD) [22] is used to calculate its pseudo-inverse. Because of the non detectable piston mode the first row only consists of zeros, therefore it makes sense to exclude this first row to have better results with the SVD algorithm. The row of zeros is added again as a leading column of  $\mathbf{Z}^\dagger$ . The piston mode can't be measured with the SH sensor thus no loss or win of information happens by leaving out the zeros.

As last step the wavefront  $W$  is obtained by first multiplying each Zernike coefficient by the according polynomial and second by superimposing the partial results, as given in matrix notation:

$$W = \mathbf{Z} \mathbf{c}_z \quad (3.12)$$

#### 3.2.5 Implementation

In this section the workflow from capturing an image with the wavefront sensor to find the subaperture spots, translating their displacements into Zernike modes and finally retrieving a 3D representation of the measured wavefront is lined out.

At first, suitable camera parameters for the SH sensor must be found. These are in particular the exposure time, the gamma correction and the region of interest. The latter describes a cut-out of the sensor area since the image sensor is bigger than the microlens array. The region of interest is found by trying to center the circular spot pattern as good as possible in the middle of the resulting image and cutting out a square with an edge length of the original image height. The other two settings,



exposure time and gamma correction, are adjusted in a way that the distinct spots are clearly visible but not overexposed since this would lead to an inaccurate wavefront reconstruction due to an inaccurate spot detection. In the presented setup the shortest possible exposure time was still too high resulting in a spot image with oversaturated pixel intensity. With the help of a polarizing filter in front of the SH sensor the intensity of the incident linear polarized laser beam is additionally decreased to avoid saturation of the spots.

To find a suitable number of utilized lenslets more system preferences must be taken into account. At first the available beam diameter of the laser together with the size of the SH sensor's aperture. And a second limitation is as described in [2, p. 68] that the highest Zernike mode that can be calculated accurately is roughly given by the number of used subapertures. This second limitation turned out to be not a very substantial problem since only modes up to the 20<sup>th</sup> are used and the number of subapertures is clearly larger than this. By laying an imaginary circle over the center of the captured spot pattern and only using the subapertures inside provides a well working solution with  $K = 132$  microlenses as displayed in Fig. 3.10.

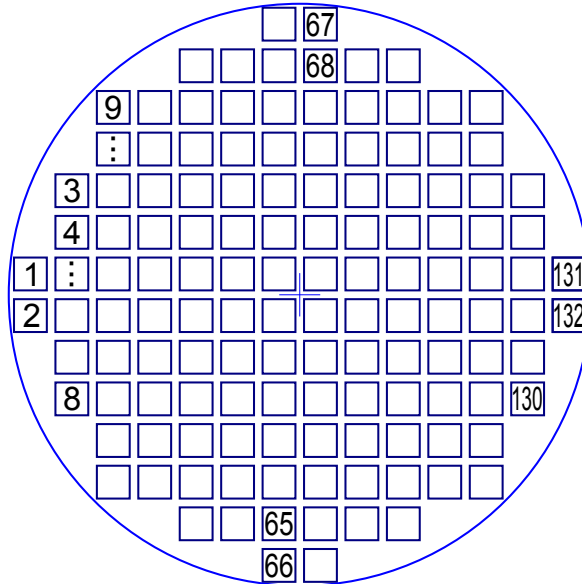


Figure 3.10: Numbering of the used lenslets. Squares symbolize the subapertures of the lens array.

Setting all preferences in an initialization routine in MATLAB<sup>®</sup> and capturing a snapshot delivers a picture as shown in Fig. 3.11 (a). The position of the subapertures are derived from a reference image whereby the four center spots (see cyan colored dots in Fig. 3.11 (c)) are utilized to define an equally spaced grid over the entire image sensor, mapping the lens array.

Spots at the rim of the laser beam are often not as bright as the center which makes them more vulnerable to noise. To get a decent wavefront reconstruction only part of the visible spots are used because limiting the used spots to the subapertures inside the circle in Fig. 3.11 (b) leads to a more robust evaluation. As seen in Fig. 3.11 (c) the blue squares represent the subapertures that are used for further processing.

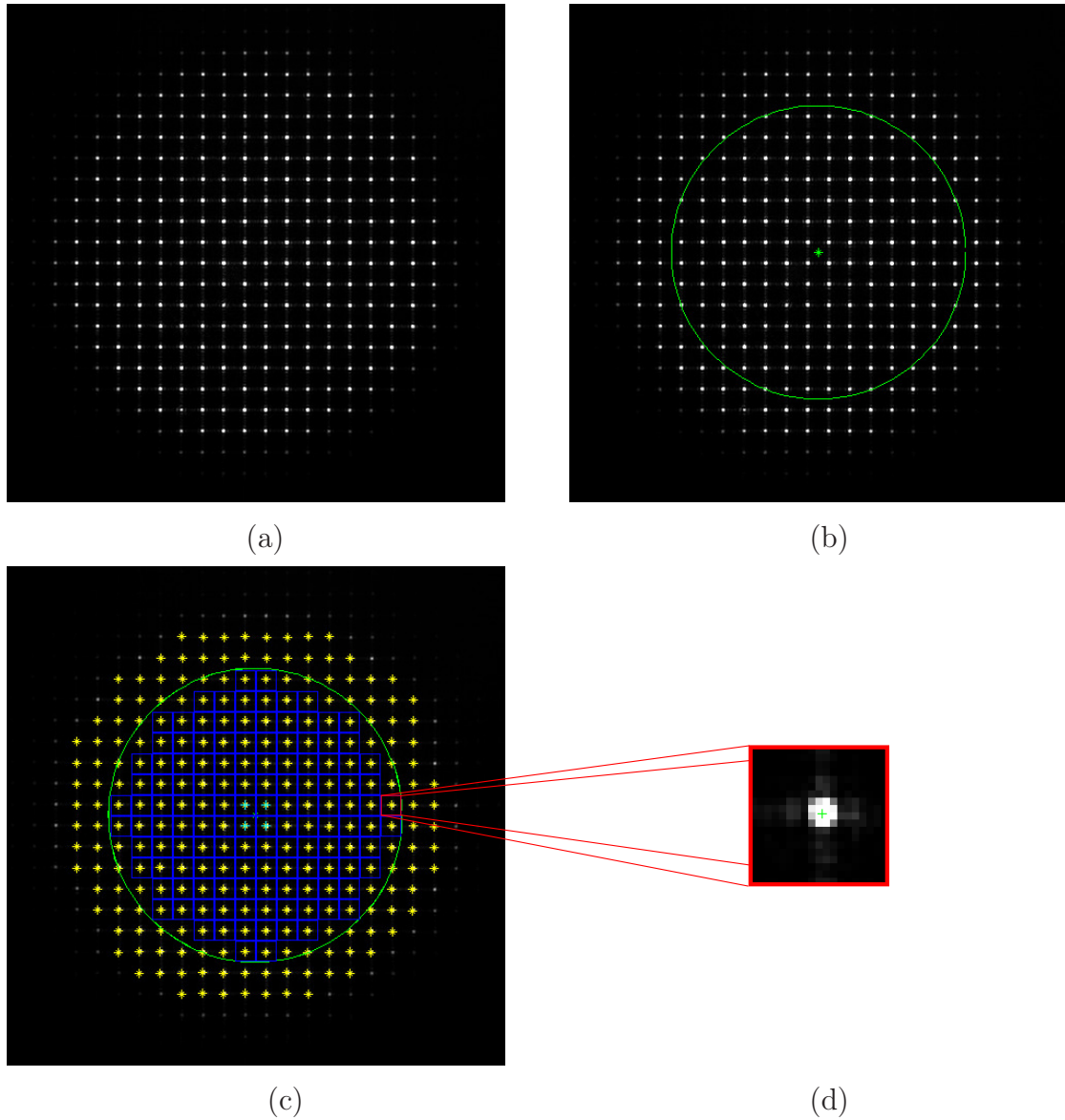


Figure 3.11: SH spot patterns. In (a) the raw image is shown while in (b) the circle with the cross (i.e. point of origin) in the center is marking the area in which the spots are evaluated. The utilized subapertures are drawn as blue squares in (c) with a yellow mark on each found spot. A magnification of one subaperture is displayed in (d) with the determined spot center (compare also Fig. 3.8).

For a first step the `bwlabel` algorithm from the MATLAB<sup>®</sup> Image Acquisition Toolbox<sup>™</sup> is used to search in the entire image for so called connected blobs and labels these. Since this algorithm is only able to detect spots in a binary image with either black or white (BW) pixels a threshold is needed. Experiments showed that 50 (in a possible range from 0 to 255) is a suitable choice for the intensity threshold. Everything below is considered as black and all above as white. With the labeling of the found blobs the function `regionprops` delivers a coarse determination of the centroids. The reason, why the so delivered centroids are not exact is that it only can compute the BW image. But in doing so, it can be checked if there are two or more spots in one subaperture. Having more than one distinct spot in a subaperture may occur when evaluating wavefronts with a SH sensor (see also Fig. 3.9). After checking if the acquired image is eligible for further processing by making sure that only one spot is within a subaperture the CoG algorithm from Eq. (3.3) is applied to every subaperture and the values for the computed centroids are stored in a vector called `snapshot_centroids`. This vector is subtracted from the vector of reference centroids which are derived from a reference image. These reference centroids represent the wavefront that the feedback controller aims for. As stated before, the so called slopes (see also Eq. (3.4) and Eq. (3.5)) are computed by dividing the difference between measured and reference centroids by the focus length of the micro-lenses. A matrix multiplication (see Eq. (3.12)) is carried out to obtain the wavefront.

### 3.3 19-channel Piezo Deformable Mirror

For the setup used in this thesis a 19-channel Piezo deformable mirror with a diameter of  $d_{DM} = 30 \text{ mm}$  from OKO Technologies is used. The surface is coated with protected silver to provide a good reflection for visible light. It is specially designed for low-order aberrations correction as stated in the technical guideline [23]. Since the exact number of Zernike modes towards which the mirror shows sufficient performance is not specified an investigation is conducted in Chapter 3.5. A photo of the used device is provided in Fig. 3.12 together with the layout of the positions of the actuators.

The layout shows a single center stack with two circles of actuators around it. The outer circle is directly on the edge of the mirror and the inner circle is slightly indented. To overcome the so called print-through effect, the two rings of actuators are outside of the used aperture of the mirror [24]. This effect is inherent to the design of normal continuous faceplate DMs as actuators causing spots in the surface when they try to form a specific shape.

All actuators are piezo stacks with a nominal stroke of  $6 \mu\text{m}$  at an input voltage of  $V_{in} = 300 \text{ V}$  (with maximum stroke of  $8 \mu\text{m}$  at  $400 \text{ V}$ ). To supply the required high-voltages and for actuation a digital to analogue converter (DAC) in combination with a high-voltage amplifier unit is used. To address each actuator with MATLAB<sup>®</sup> a custom programmed C-function is implemented, based on the supplied application programming interface (API). The C-function is compiled into a MEX-function to have the ability to call it as any common MATLAB<sup>®</sup> function.

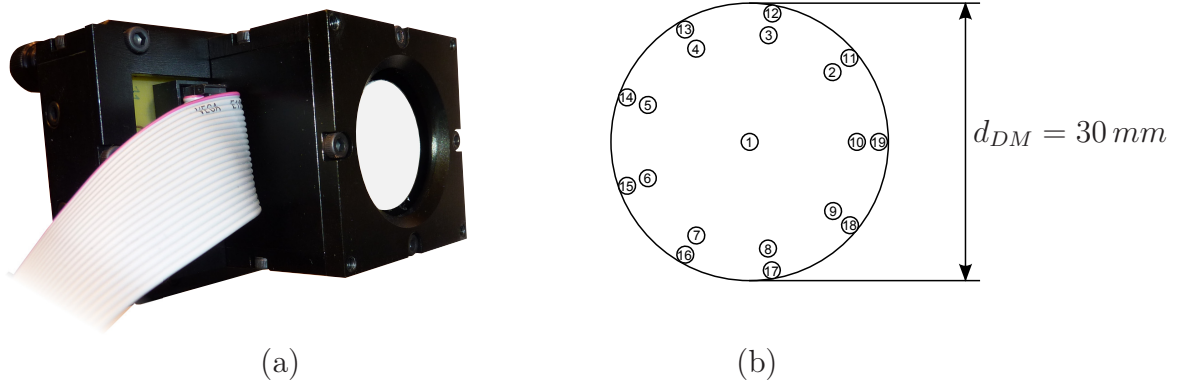


Figure 3.12: Photo of the used DM in (a) with the arrangement of the 19 piezo actuators in (b). Characteristic for this type is the single center stack complemented by two rings along the rim.

### 3.4 Feedback Control Algorithm

In general piezo actuators are suffering from a relatively strong hysteresis due to their inner polarization effects. The absolute error for feed forward positioning of a piezo stack depends on the applied voltage (i.e. the electric field) and is between 2% and 15% of the nominal displacement according to [25]. Therefore the performance of the deformable mirror is strongly connected to a suitable feedback control algorithm to cope with nonlinearities, model uncertainties and to make sure that the real surface deflection converges to the desired one.

Before feedback algorithms are described, the concept of the influence matrix  $\mathbf{A}$  is presented. The influence matrix describes the mapping of the actuators movement, expressed by the applied (normalized) voltage  $\mathbf{v}$  to the resulting deformation of the mirrors surface, expressed by the measured slopes  $\mathbf{s}$ .

$$\mathbf{s} = \mathbf{A}\mathbf{v} \quad (3.13)$$

To determine  $\mathbf{A}$  for the actual setup it is possible to apply the maximum voltage to each actuator separately (i.e.  $\mathbf{v}_1 = [1, 0, 0, \dots]^T$ ,  $\mathbf{v}_2 = [0, 1, 0, \dots]^T$ ) and measure the resulting slopes ( $\mathbf{s}_{v1}$ ,  $\mathbf{s}_{v2}, \dots$ )

$$\mathbf{A} = \mathbf{S}\mathbf{V}^{-1} = \left( \begin{bmatrix} \mathbf{s}_{v1} \\ \vdots \end{bmatrix}, \begin{bmatrix} \mathbf{s}_{v2} \\ \vdots \end{bmatrix}, \dots \right) \left( \begin{bmatrix} \mathbf{v}_1 \\ \vdots \end{bmatrix}, \begin{bmatrix} \mathbf{v}_2 \\ \vdots \end{bmatrix}, \dots \right)^{-1} = \quad (3.14)$$

$$= \left( \begin{bmatrix} s_{v1} \\ \vdots \end{bmatrix}, \begin{bmatrix} s_{v2} \\ \vdots \end{bmatrix}, \dots \right) \begin{pmatrix} 1 & 0 & \dots & 0 \\ 0 & 1 & \dots & 0 \\ \vdots & \vdots & \ddots & \vdots \\ 0 & 0 & \dots & 1 \end{pmatrix} \quad (3.15)$$

such that the collected voltage vectors form the identity matrix and therefore  $\mathbf{A}$  is

the composition of the measured slopes. This method assumes a linear relationship between the actuator deflection and the measured slopes over the full range.

Measurements showed that only the region between 20 % and 80 % of the maximum actuator voltage leads to a linear relation between  $\mathbf{v}$  and  $\mathbf{s}$ . A different approach uses a large number of measurements with random voltage vectors  $\mathbf{v}$  with all voltage values inside the linear region. In the actual setup this method was used with a total number of 264 measured actuator-slope relations. The influence matrix is then derived from:

$$\mathbf{A} = \mathbf{S}\mathbf{V}^\dagger \quad (3.16)$$

The condition number of a non-quadratic matrix gives a hint on how close the pseudo-inverse comes to the solution of a set of linear equations. With the described method of finding  $\mathbf{A}$  a condition number for the matrix  $\mathbf{V}^\dagger$  smaller than 10 was achievable which is comparable sufficient value.

With the use of the influence matrix  $\mathbf{A}$  a commonly used feedback function is similar to a simple integrator described in [26]:

$$\mathbf{s}_d = \mathbf{Z}\mathbf{c}_z \quad (3.17)$$

$$\mathbf{v}_{n+1} = \mathbf{v}_n - g\mathbf{A}^\dagger(\mathbf{s} - \mathbf{s}_d) \quad (3.18)$$

Where the desired slopes  $\mathbf{s}_d$  are computed by using the reconstruction matrix  $\mathbf{Z}$  and the desired Zernike coefficients  $\mathbf{c}_z$ . The resulting voltage vector  $\mathbf{v}_{n+1}$  is the previous one  $\mathbf{v}_n$  with a subtracted error. The error consists of the difference of the desired to the measured slopes multiplied by the pseudo-inverse of the influence matrix  $\mathbf{A}^\dagger$  and an integrator gain  $g$ . The problem with this algorithm is the explicit usage of the pseudo-inverse which is in some cases not very robust, depending on the singular values of  $\mathbf{A}$ . Small defects in  $\mathbf{A}$  could lead to enormous changes in  $\mathbf{A}^\dagger$ . First experiments have shown that the algorithm in Eq. (3.18) is not capable to deliver the desired performance concerning speed, accuracy and convergence.

In [27] an alternative feedback control algorithm is presented which has been developed for a push pull mirror. It is based on an iterative learning control (ILC) algorithm by trying to minimize the error for the next step  $\mathbf{e}_{n+1}$ , formulated as optimization problem. The solution of the optimization problem is:

$$\mathbf{e}_n = \mathbf{s}_d - \mathbf{s} \quad (3.19)$$

$$\mathbf{v}_{n+1} = \mathbf{v}_n + (\mathbf{A}^T\mathbf{A} + \beta\mathbf{I})^{-1}\mathbf{A}^T\mathbf{e}_n \quad (3.20)$$

The error  $\mathbf{e}_n$  is found by the difference between the desired slopes  $\mathbf{s}_d$  and the measured slopes  $\mathbf{s}$ . The iteratively computed voltage vector for the next step  $\mathbf{v}_{n+1}$  is based on the previous one with an addition of the error multiplied by a factor similar to Eq. (3.18). The influence of the regularization parameter  $\beta$  (with  $0 < \beta < 1$ ) on the behavior of the AO system is investigated in Chapter 3.5.1 in detail. In advance it can be said that by choosing  $\beta$  close to one a slow convergence speed is expected while a smaller  $\beta$  increases the convergence speed with the risk of causing oscillations. Even though this feedback algorithm was originally designed for a push-pull MMDM it fitted very well for the proposed setup and showed good performance.

## 3.5 Results 1: Control Capabilities

This section provides the results of the investigations of the built AO setup. Starting with the finding of a suitable regularization parameter  $\beta$  followed by an investigation of the capabilities of the adaptive optics system to work in a feedback configuration. This is tested by forming distinct Zernike modes with the DM and measuring the output wavefront with the Shack-Hartmann sensor.

In Fig. 3.13 a photo of the setup is displayed. It shows the main components of the AO system working in a feedback loop. The laser beam hits the beam splitter from the right, goes through the beam expander formed by  $L_1$  and  $L_2$  and is reflected back by the DM. For protection the DM is covered on the photo (compare Fig. 3.12). The light goes straight back through the two lenses (now working as a beam concentrator) and is reflected by the beam splitter towards the SH wavefront sensor. Between the two lenses a polymethyl methacrylate, acrylic glass or Plexiglas<sup>®</sup> (PMMA) disk introduces static aberrations.

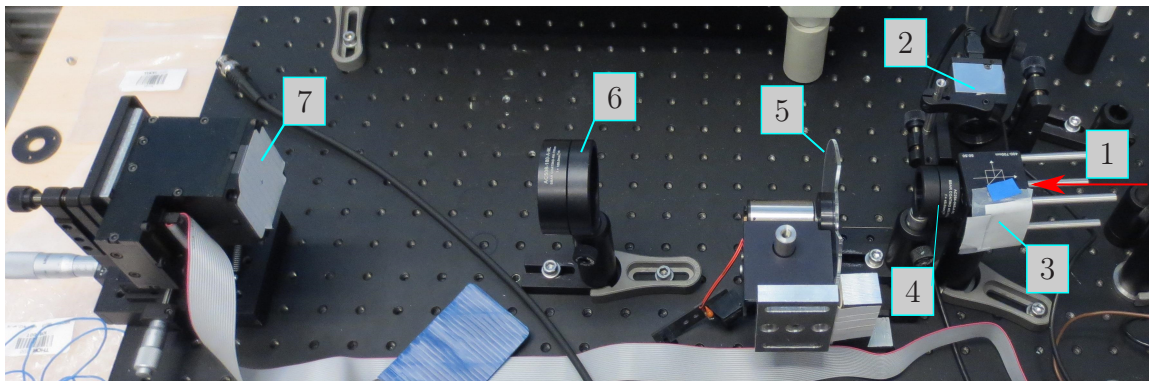


Figure 3.13: Photo of the adaptive optics part of the setup.

The descriptions of the labels for Fig. 3.13 are as follows:

1. incoming laser beam
2. Shack-Hartmann sensor
3. beam splitter
4. lens  $L_1$ ,  $f_1 = 45$  mm,
5. PMMA disk as disturbance,
6. lens  $L_2$ ,  $f_2 = 180$  mm,
7. deformable mirror (surface is covered for protection)

The special layout of the AO system differs from the basic schematic in Fig. 3.1. That is the case because it is integrated into the interferometer setup that is investigated in the following chapter. Since alignment is crucial the measurement for the AO part was carried out in the combined setup which will be presented later.

### 3.5.1 Regularization Parameter

As discussed in Chapter 3.4 the used algorithm for feedback control of the AO system is

$$\mathbf{e}_n = \mathbf{s}_d - \mathbf{s} \quad (3.21)$$

$$\mathbf{v}_{n+1} = \mathbf{v}_n + (\mathbf{A}^T \mathbf{A} + \beta \mathbf{I})^{-1} \mathbf{A}^T \mathbf{e}_n \quad (3.22)$$

with the error  $\mathbf{e}_n$ , the desired slopes  $\mathbf{s}_d$  and the measured slopes  $\mathbf{s}$ .  $\mathbf{v}$  stands for the (normalized) voltage applied to the piezo actuators of the mirror,  $\mathbf{A}$  is the influence matrix,  $\beta$  denotes the regularization parameter and  $\mathbf{I}$  represents the identity matrix.

To find an appropriate regularization parameter  $\beta$  (with  $0 < \beta < 1$ ) a constant disturbance was introduced into the measurement path. The RMS value of the measured wavefront compared to a flat wave was monitored while the controller tried to compensate for the disturbance.

The disturbance is shown in Figure 3.14 as an interferogram on the left together with a three dimensional representation on the right.

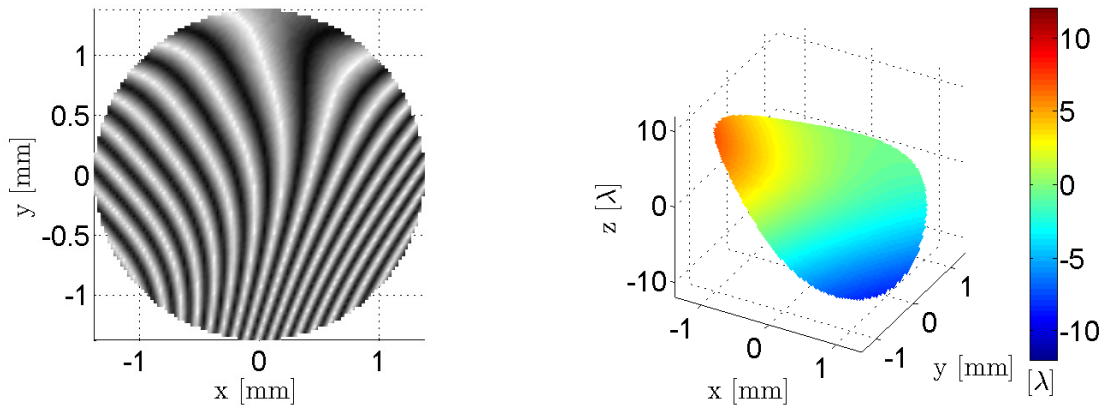


Figure 3.14: Interferogram and 3D wavefront representation of the applied disturbance.

The associated Zernike coefficients of this disturbance are displayed in Fig. 3.15. The strongest modes are vertical tilt, the first astigmatism and defocus.

A decomposition up to the 20<sup>th</sup> Zernike mode shows that considerable modes only appear up to mode 9.

If now the feedback control is applied to this sample disturbance the RMS value of the measured wavefront is monitored. Performing the measurements with different regularization parameters  $\beta$  shows, that for values between 0,001 and 1 the algorithm shows a faster convergence and a smaller residual RMS error if  $\beta$  is smaller. However, when using  $\beta = 0,0001$  the control algorithm shows a fast convergence only at the beginning, followed by an oscillation before reaching a higher final RMS value compared to  $\beta = 0,0015$ .

The curves in Fig. 3.16 shows that the regularization parameter cannot be chosen as small as possible for obtaining the smallest final residual RMS error. Too small values of  $\beta$  result in a higher residual error. Such a behavior can be explained when referring to the L-curve plot of a numerical inverse problem for solving  $Ax_\lambda = b$ , as described

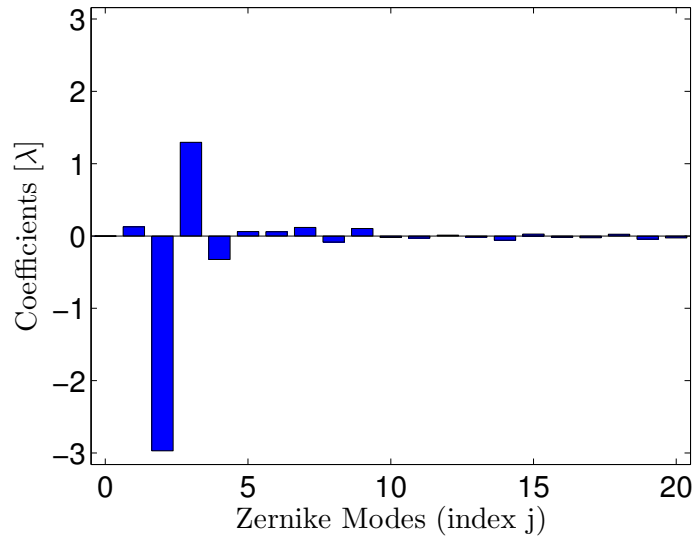


Figure 3.15: Zernike modes with their corresponding weighting coefficients of the applied disturbance from Fig. 3.14.

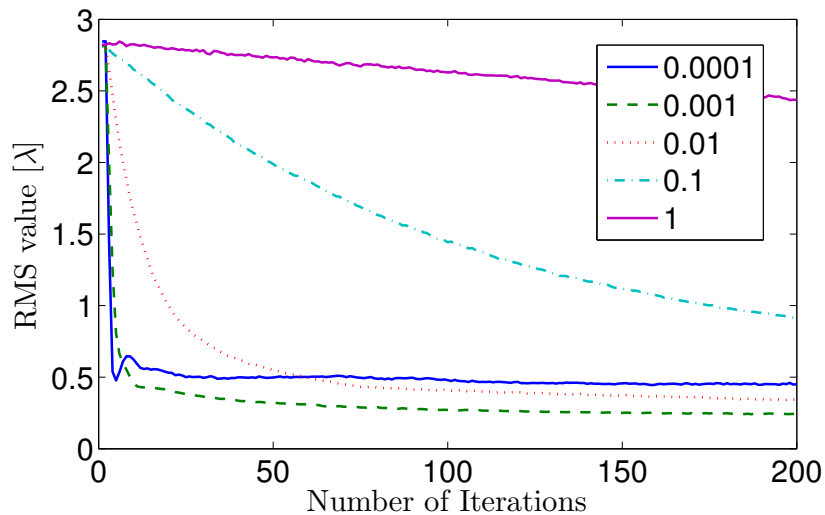


Figure 3.16: Comparison of different regularization parameters  $\beta$ . The ordinate depicts the RMS value of the measured wavefront and the abscissa shows the iteration cycles of the feedback controller.

in [28]. The L-curve displays the norm of the regularized solution ( $\|x_\lambda\|_2$ ) against the norm of the residual ( $\|Ax_\lambda - b\|_2$ ) when changing the regularization parameter. An example is depicted in 3.17.

On one hand, a large regularization parameter shows a high residual  $\|Ax_\lambda - b\|_2$  since it does not fit the given data  $b$ . On the other hand, a small regularization parameter leads to a nice fit of the residual  $\|Ax - b\|$ , but the solution will suffer from data and numerical errors, so  $\|x_\lambda\|_2$  will be large. The latter applies to the behavior depicted in Fig. 3.16 where  $\beta = 0,0001$ , causing a larger RMS error compared to  $\beta = 0,001$ .



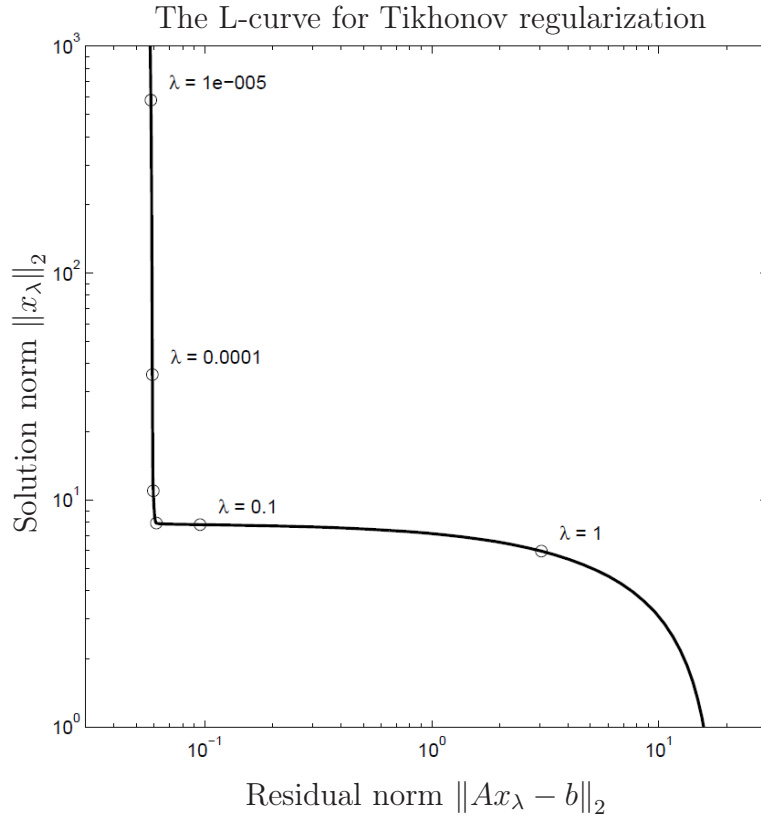


Figure 3.17: L-curve of a numerical inverse problem. A regularization method (e.g. Tikhonov regularization) is applied for solving the inverse problem. The L-curve describes the trade-off between the size of a regularized solution and its fit to the given data [28].

So far the measurement was only carried out with one specific aberration. To find a proper  $\beta$  a series of tests is conducted with three different values for the regularization parameters in five disturbances, namely G1 to G5. The applied disturbances are displayed in Appendix 1 and an overview on the initial RMS and peak-to-valley (P-V) values is given in Table 3.2.

Table 3.2: Initial RMS and P-V values of the applied disturbances.

Disturbance	RMS	P-V
# G1:	2,7498 $\lambda$	14,9925 $\lambda$
# G2:	1,5442 $\lambda$	6,2694 $\lambda$
# G3:	2,1713 $\lambda$	9,6288 $\lambda$
# G4:	2,9856 $\lambda$	13,6309 $\lambda$
# G5:	2,0189 $\lambda$	8,1933 $\lambda$

The disturbances all have a dominant tip/tilt (modes 1 and 2) and in decreasing order astigmatism (mode 3, 5), defocus (4), trefoil (6, 9) and coma (7, 8). This kind of distribution was characteristic for all introduced disturbances.

As an example, how the measurement was executed the graph in Fig. 3.18 shows

the trace of the RMS value of disturbance number G1 over 1200 controller iterations with three different regularization parameters. For a better meaningfulness the graph is vertically zoomed in to see that a regularization parameter of  $\beta = 0,0015$  (in - - - green) leads to the best result in meanings of the residual RMS value even though it looks a little bit slower in the beginning. The starting value of the RMS error is about two decimal powers bigger than the residual error.

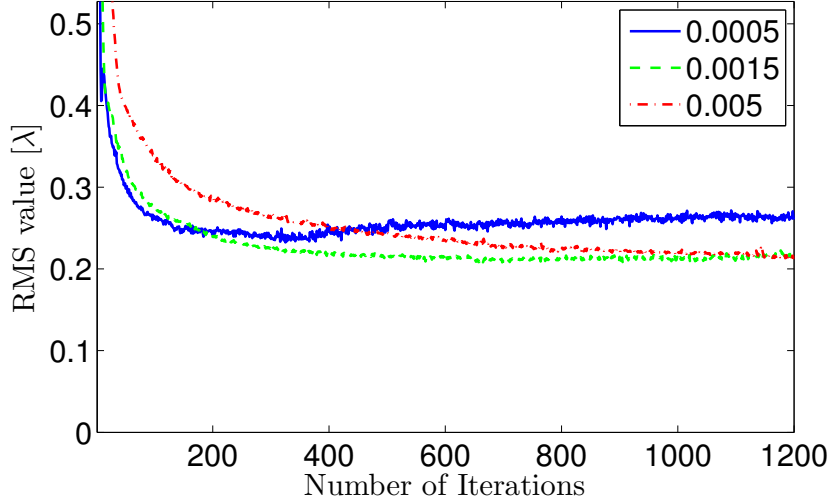


Figure 3.18: Longrun of the RMS measurement for disturbance G1 with three different regularization parameters  $\beta$ .

The second thing to look at, besides the RMS and the P-V value, is the convergence speed of the controller, or in other words, how many iterations are needed to have a final value that is in a 1% range of an assumed asymptotic value.

As conclusion a regularization parameter of  $\beta = 0,0015$  is a qualified choice in terms of a decent convergence speed of the feedback algorithm and smoothly approaching the final shape. At approximately 600 iterations the output can be considered as constant if the disturbance is kept static.

### 3.5.2 Zernike Mode Forming Ability

As next step the capability of the AO system to form designated Zernike modes is tested. Forming specific Zernike modes is important since any disturbance is assumed to be a superposition of a finite number of modes. First a feedforward approach is used to calculate initial values of the output voltage vector  $\mathbf{v}$ :

$$\mathbf{s}_d = \mathbf{Z} \mathbf{c}_z \quad (3.23)$$

$$\mathbf{v} = \mathbf{A}^\dagger \mathbf{s}_d. \quad (3.24)$$

With the slope vector  $\mathbf{s}_d$ , the reconstruction matrix  $\mathbf{Z}$ , the influence matrix  $\mathbf{A}$  and the (desired) Zernike coefficient vector  $\mathbf{c}_z$ .

The voltage vector is applied to the piezo actuators of the mirror before the feedback control is started to compensate for not modeled effects such as hysteresis. The

maximum value of the Zernike coefficient is limited by the applicable voltage. Computing the voltage vector for higher indices  $j$  shows that the possible maximum value of the coefficients decreases because  $\mathbf{v}$  goes earlier into saturation. In other words, lower modes can be formed with considerably stronger gain than higher modes. Thus, the Zernike coefficient  $c_z$  was chosen so that the magnitudes of the elements of the voltage vector  $\mathbf{v}$  never exceeded 85 % of their upper limit. This limit provides some margin to the top value for the feedback controller and it is in the linear region of the mirror. To have a characteristic value for how clear one mode  $j$  can be formed by the mirror the metric of the purity  $P_j$  was used (see Chapter 2.4).

As an example, the third mode (i.e. the first astigmatism) is picked out to show the approach. The iterative calculation of the initial  $\mathbf{v}$  results in a gain factor of  $c_{z3} = 7,4620 \times 10^{-7} \text{ m} \cong 1,18 \lambda$ . Fig. 3.19 shows the calculated actuator voltages.

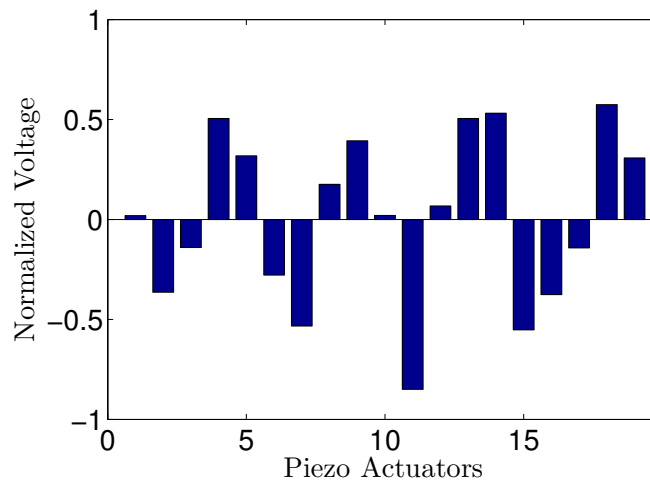


Figure 3.19: Calculated voltage vector  $\mathbf{v}$  for a Zernike coefficient  $c_{z3} = 7,4620 \times 10^{-7} \text{ m}$ . The magnitudes of the maximum voltages are all within  $\pm 0,85$ .

After applying the feedback algorithm, the saddle-like shape of astigmatism can be observed, as shown in Fig. 3.20.

The purity of the shape with  $P_3 = 0,9994$  indicates a good forming capability. The appearance of other modes is negligible, as shown in Fig. 3.21.

Following the presented example, the forming capability of the first 16<sup>th</sup> modes is analyzed in the next step. In Fig. 3.22 all maximum coefficients for each Zernike mode are displayed. The conducted experiments showed that an investigation up to the 16<sup>th</sup> mode is enough because no proper forming of any higher mode was possible.

On one hand, a general decrease of the coefficients of higher modes is noticeable and on the other hand that columns mainly show up in pairs. The latter is a consequence of the fact that modes with a distinct symmetry plane always appear with a complementary mode perpendicular to it. Only modes like defocus (mode  $j = 4$ ) with a rotational symmetry are without any direct opponent. To explain why one tilt (and one astigmatism) is bigger than the other it must be stated that alignment is crucial in the whole setup and even a small tilt in a mounting of the optical components could cause one direction to be favored over the other. The other observation is that the coma related modes are harder to form for the system. The first two coma modes (7

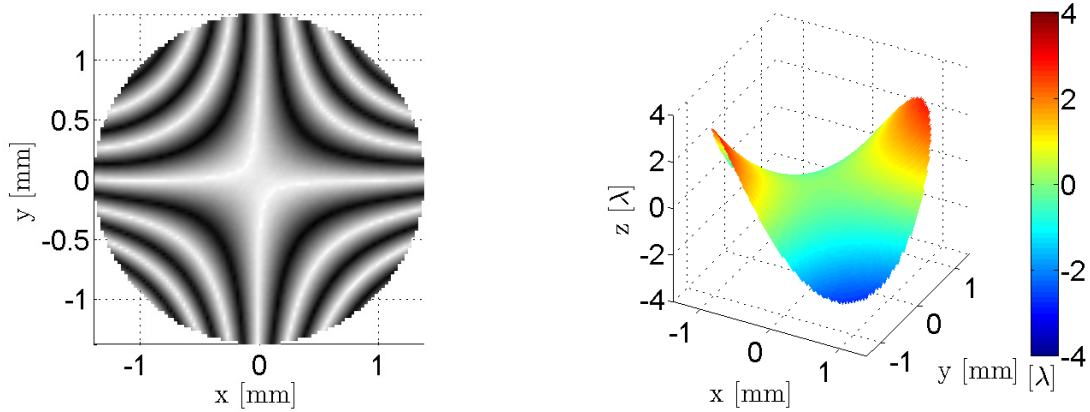


Figure 3.20: Interferogram (left) and saddle-like shaped 3D representation (right) of the first astigmatism (i.e. Zernike mode  $j = 3$ ).

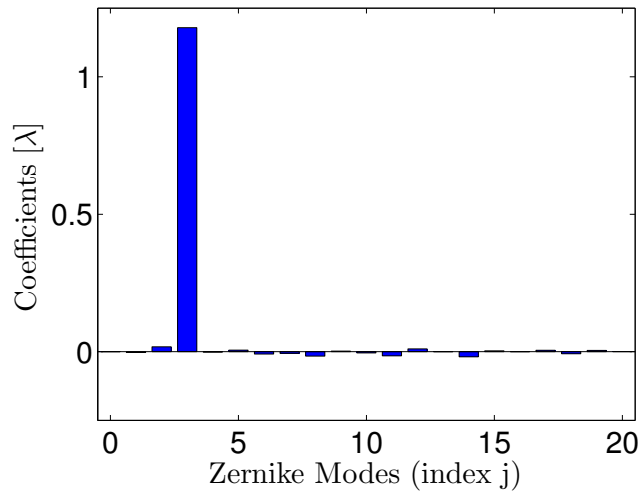


Figure 3.21: Depiction of the measured Zernike coefficients when trying to get the best forming of the third Zernike mode. Obviously the third coefficient is dominant, but still some other modes appear to be non-zero.

and 8) as well as the secondary astigmatism (11 and 13) are considerably smaller than the previous or the following modes, respectively. A reason of this behavior lies in the geometry of the mirror and the attached actuators which are designed in a way to be able to form the edge of the mirror more than building hills and valleys inside the surface.

Another important graph rating the forming capabilities is shown in Fig. 3.23 where the purity value for each single mode is displayed.

The measurement for every mode was done separately and it can be seen that the first six modes are reconstructed very pure (see also Fig. 3.21) while in the higher modes also other coefficients are induced and therefore the purity decreases. The graph also shows that only modes up to the 15<sup>th</sup> mode are presentable with a positive coefficient and purity. The 16<sup>th</sup> mode is not representable at all.

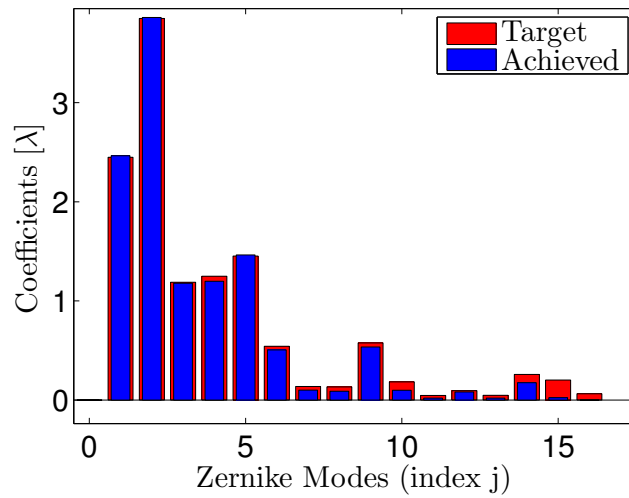


Figure 3.22: Forming of distinct modes. Red bars in the background represent calculated target values while blue bars in the front are the achieved ones.

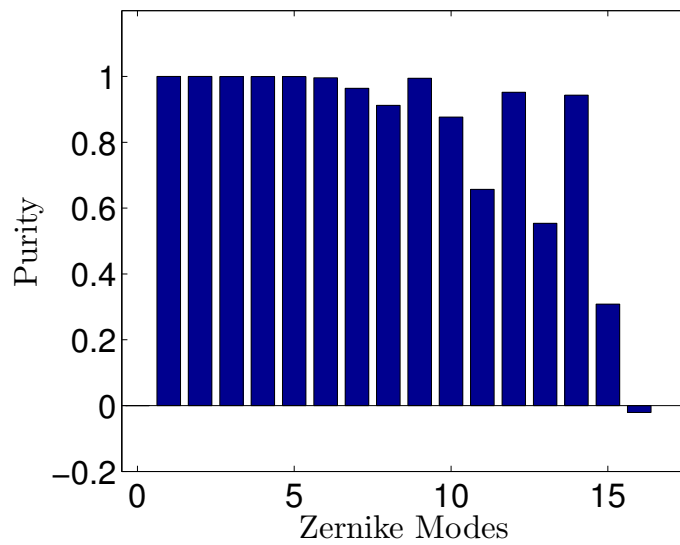


Figure 3.23: Purity  $P_j$  of the Zernike modes. Each value is computed for a distinct mode separately and then brought together in one bar-diagram.



---

## Interferometer System

---

This chapter outlines the interferometer principle together with the characteristics and practical issues of a Michelson interferometer. Additionally, some of the improvements that were developed to cope with its imperfections are presented. The last two sections describe the achieved results if the adaptive optics system is integrated into the Interferometer setup together with an conclusion derived from the measurements results.

Interferometric measurements are used in a variety of fields that include astronomy, chemistry, physics and especially one major application area, the high precision distance metrology. According to [29], one of the main advantages of interferometer metrology is the ability to gain precise position information without changing the system's dynamics. Interferometry can be considered as non-contact method and in most cases only a (lightweight) mirror plate has to be mounted on the measuring object. Therefore it can be easily combined in a feedback loop to allow high precision positioning. For example in the chip manufacturing industry where the exact positioning for silicon wavers is the main usage [30]. Similar to this, the production process of LCD screens also relies heavily on interferometer precision. Other applications are found for example in the field of calibration for other measurement devices or machine tools.

### 4.1 Interferometer Principle

In general interference of waves from a coherent light source comes as a consequence of the superposition principle. Two waves of equal frequency and polarization but different phase are defined as:

$$\vec{E}_1 = \hat{\mathbf{E}}_1 \cos(\omega t + \theta_1) \quad (4.1)$$

$$\vec{E}_2 = \hat{\mathbf{E}}_2 \cos(\omega t + \theta_2) \quad (4.2)$$

with  $\hat{\mathbf{E}}_1$ ,  $\hat{\mathbf{E}}_2$  being the amplitude and  $\theta_1$ ,  $\theta_2$  representing the phase. The net electric field at a certain location is now the algebraic sum of the two waves. Assuming they

#### 4 Interferometer System

both have the same electric field strength amplitude  $\hat{\mathbf{E}}_1 = \hat{\mathbf{E}}_2 = \hat{\mathbf{E}}$  together with  $\theta_1 = 0$  and  $\theta_2 = \Delta\theta$ , with no loss in generality, results in a net electric field:

$$\vec{E}_{net} = \vec{E}_1 + \vec{E}_2 \quad (4.3)$$

$$= \hat{\mathbf{E}} (\cos(\omega t) + \cos(\omega t + \Delta\theta)) = \quad (4.4)$$

$$= 2\hat{\mathbf{E}} \left( \cos\left(\omega t + \frac{\Delta\theta}{2}\right) \cos\left(\frac{\Delta\theta}{2}\right) \right) \quad (4.5)$$

As a result from the trigonometric addition theorem, the sum of the two sinusoidal signals transfers to a multiplication with a term  $\cos\left(\frac{\Delta\theta}{2}\right)$  which has its maximum at  $\Delta\theta = 0$  and is zero at  $\Delta\theta = 180^\circ$ . By introducing the amplitude of the net electric field

$$\hat{\mathbf{E}}_{net} = 2\hat{\mathbf{E}} \cos\left(\frac{\Delta\theta}{2}\right) \quad (4.6)$$

it can be seen that the amplitude varies from twice the amplitude of one of the beams to zero, depending on the phase shift between the two interfering beams. The frequency-dependent term  $\cos\left(\omega t + \frac{\Delta\theta}{2}\right)$  shows a net phase shift of half of the original  $\Delta\theta$ . An example is shown in Fig. 4.1 where the constructive interference at  $\Delta\theta = 0$  shows double the amplitude of the single waves. With increasing phase shift the amplitude decreases until  $\Delta\theta = 180^\circ$  where they cancel each other out, also known as destructive interference.

Since the optical frequencies are too high for electronics in a practical use the electric field is not evaluated directly. Instead, the irradiance  $I_{r,c}$  is used, where the  $\cos\left(\omega t + \frac{\Delta\theta}{2}\right)$  term in Eq. (4.5) is averaged out by the integration time of the detector. The irradiance of the net electrical field of two interfering light beams is provided by

$$I_{r,c} = \frac{c_0 n \varepsilon_0}{2} \hat{\mathbf{E}}_{net}^2 \quad (4.7)$$

with the speed of light  $c_0 = 299\,792\,458$  m/s, the refraction index of the surrounding atmosphere  $n$  (e.g. for air  $n \cong 1,000292\dots$ ) and the vacuum permittivity  $\varepsilon_0 \cong 8,8542 \times 10^{-12}$  F/m. By using the net amplitude from Eq. (4.6) it follows to:

$$I_{r,c} = \frac{c_0 n \varepsilon_0}{2} \left( 2\hat{\mathbf{E}} \cos\left(\frac{\Delta\theta}{2}\right) \right)^2 = c_0 n \varepsilon_0 \hat{\mathbf{E}}^2 (1 + \cos(\Delta\theta)) \quad (4.8)$$

Comparing this value with the irradiance delivered by only one beam

$$I_{r,1} = I_{r,2} = I_r = \frac{c_0 n \varepsilon_0}{2} \hat{\mathbf{E}}^2 \quad (4.9)$$

shows that the measured irradiance is in case of constructive interference (i.e.  $\Delta\theta = 0$ ) four times bigger than the irradiance of a single beam. In case of destructive interference (i.e.  $\Delta\theta = 180^\circ$ ) the acquired signal is zero:

$$I_{r,c} = \begin{cases} 2c_0 n \varepsilon_0 \hat{\mathbf{E}}^2 = 4I_r & \text{if } \Delta\theta = 0 + 2\pi k \\ 0 & \text{if } \Delta\theta = \pi + 2\pi k \end{cases} \quad (4.10)$$



Fig. 4.1 provides also the values of  $I_{r,c}$  next to the plotted electric field.

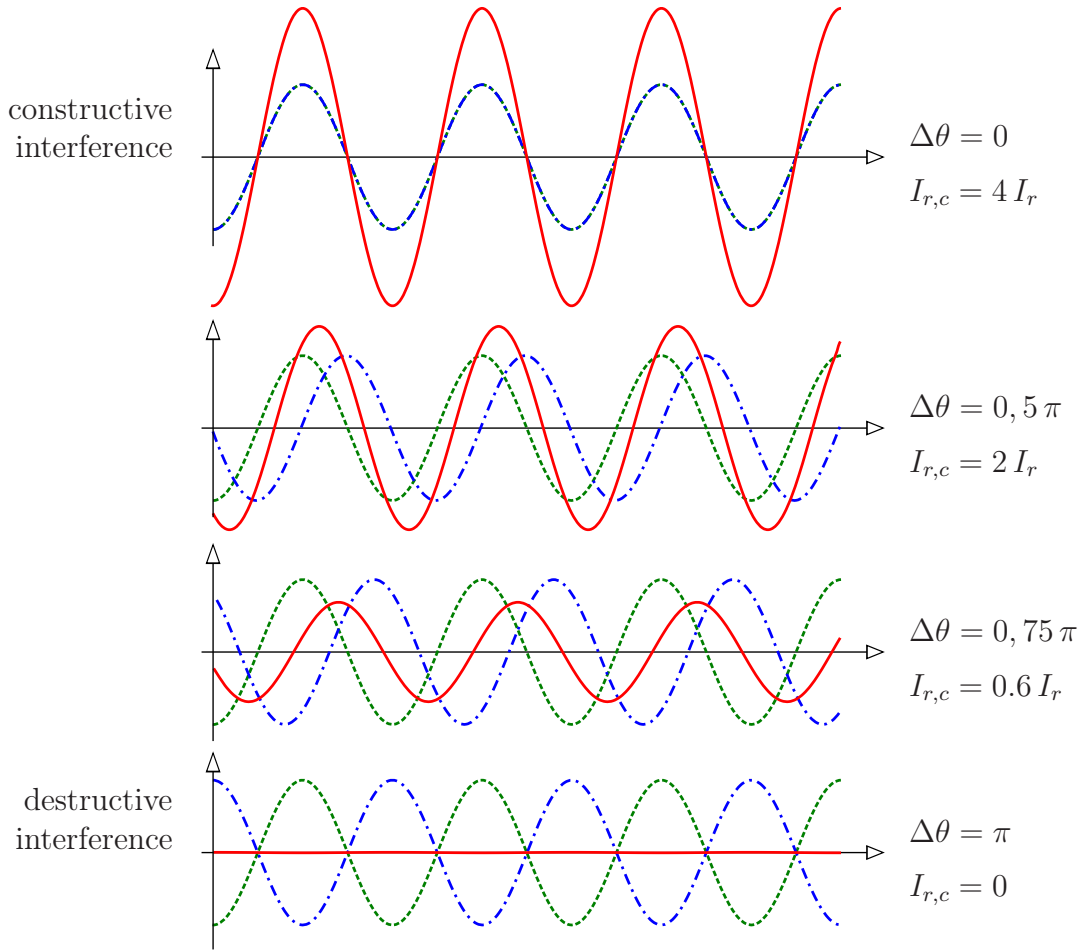


Figure 4.1: Two waves (blue and green) with increasing phase difference  $\Delta\theta$  interfere with each other. The amplitude of the interfered electric field (red) is dependent on the phase difference between the two waves and is zero for  $\Delta\theta = \pi$  (destructive interference) and twice the electric amplitude of the single wave for  $\Delta\theta = 0$  (constructive interference).

Assuming plane waves and using a photo detector to measure the interference signal the output voltage  $V_D$  of the photo detector is a product of the irradiance  $I_{r,c}$ , the wavelength-dependent optical power to electrical current efficiency factor  $\eta_\lambda$ , the transimpedance amplifier gain  $G$  and the utilized sensor area  $A_D$ :

$$V_D = \eta_\lambda G I_{r,c} A_D \quad (4.11)$$

A transimpedance amplifier is needed to convert the photocurrent, delivered from the sensor surface of the photo detector, into a voltage, which can be processed further for example by an analogue to digital converter (ADC).

## 4.2 Basic Michelson Interferometer

A setup of the homodyne (i.e. single frequency) Michelson interferometer is shown in Fig. 4.2.

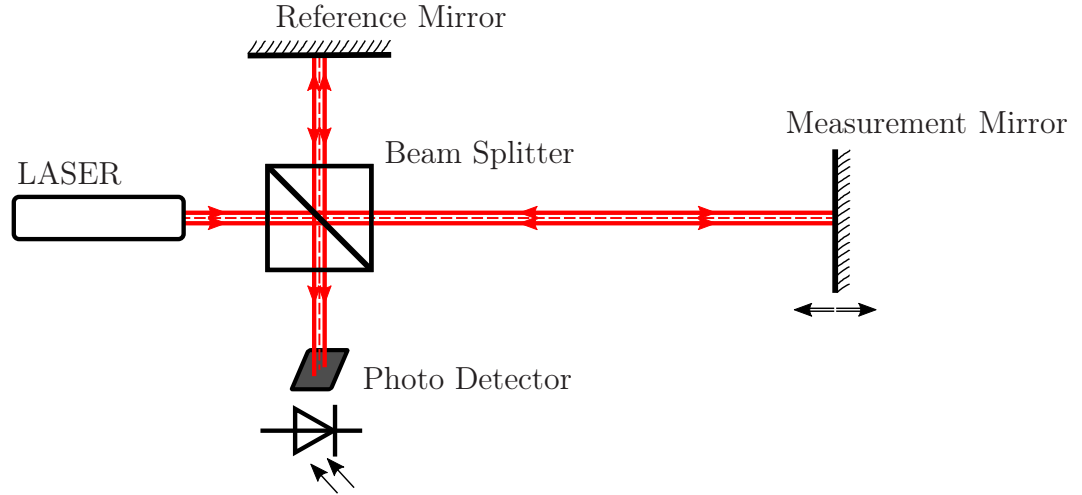


Figure 4.2: Schematic of a homodyne Michelson interferometer setup. The laser source provides a coherent laser beam while the beam splitter separates them into a reference path (up) and a measurement path (right). Both are reflected by mirrors and at the output of the beam splitter (downwards) the interference signal can be recorded.

The laser sends out a collimated beam of coherent light with one frequency. A beam splitter comprising a half-transparent mirror divides the incoming laser beam into a reference and measurement path. The beam in the reference path is reflected by the reference mirror whereas the beam in the measurement path is reflected by the measurement mirror that is attached to a moving object for measuring relative distances. Both beams interfere with each other after they are merged by the same beam splitter.

Moving the object in orders of the used wavelength causes an optical path length (OPL) that equals the phase difference:

$$\Delta\theta = \frac{2\pi}{\lambda} 2\Delta x \quad (4.12)$$

The displacement of the measurement object  $\Delta x$  is multiplied by two because the beam has to go back and forth. This OPL leads to an output voltage of the photo-detector depending on the moved distance of the measurement mirror (compare Eq. (4.8) and Eq. (4.11), with all constant parameters summed up in  $K$ ):

$$V_D = K \left( 1 + \cos \left( \frac{4\pi \Delta x}{\lambda} \right) \right) \quad (4.13)$$

If all parameters, except the phase difference, are assumed to be constant, the output

is only dependent on the change of the OPL of the measurement path which in this case is equivalent to twice the movement of the object parallel to the direction of the laser beam. For example, if the used laser has a wavelength of  $\lambda = 633 \text{ nm}$  and the object would move a quarter of a wavelength, the resulting change of the OPL is  $\lambda/2$ .

$$\Delta x = \lambda/4 = 158,25 \text{ nm} \quad (4.14)$$

$$\Delta OPL = \lambda/2 = 316,50 \text{ nm} \quad (4.15)$$

$$\Delta\theta = \pi \quad (4.16)$$

When constantly moving the object, a transition from the maximum of the signal to zero is measured, leading to a sinusoidal output. By counting the recorded minima (or equivalent to that, the maxima) the traveled distance of the object can be computed by multiplying this number with  $\lambda/2$  of the used laser. With this method the measurement range is only limited by the coherence length of the laser which makes it a powerful method for high-precision positioning over a comparable long distance.

The description above is only valid if all parameters in Eq. (4.8) and in particular the refraction index  $n$ , are constant. Since the interferometer only measures the OPL a local change of  $n$  within the measurement path, as it can occur with air turbulences, also influences the measurement. By only observing the output of the interferometer it is not identifiable if the change of the OPL originates from a movement of the measurement object or a change of the refraction index within the path, thus making the measurement result sensitive to changes in the optical path.

### 4.2.1 Improvements for High-Precision Distance Measurement

From the first trials to modern industrial measurement devices a lot of enhancements were introduced. Starting from the basic setup of a Michelson interferometer with a homodyne laser, one beam splitter, two mirrors and one detector (see Fig. 4.2), modern systems can be far more complex. The most important enhancements concerning usability and increase of robustness are as follows [29]:

- Detection of moving direction: According to Eq. (4.13), the actual moved distance can be measured by counting minima (or maxima) of the acquired signal, however the direction of movement is still unknown. By introducing a second detector after an additional beam splitter and a  $90^\circ$  phase delay the direction of movement can be determined. As depicted in Fig. 4.3, if now one detector is at a minimum (or maximum) the other one is at a phase with the biggest gradient showing a decrease or increase of the signal and thus the direction of movement can be derived.
- Reducing loss of intensity with polarizing beam splitter (PBS): When the laser beam is divided the first time at the beam splitter, 50 % of the light goes in each direction. Assuming the reference and the measurement mirrors reflect the light ideally each beam hits again the beam splitter with only 50 % of the incoming intensity going towards the output and the other half is send back into the direction of the laser (which can also cause error inside the cavity of the laser).

## 4 Interferometer System

To cope with this, two orthogonal light polarizations are used, emitted by the same light source. Together with a PBS it is possible to split  $p$  and  $s$  polarized light into two paths. With the help of so called Quarter Wave Plates ( $\lambda/4$ -WP) at the exit of the PBS it's possible to change a linear polarization into circular polarization which is then reversed at the mirrors. When coming back from the mirror, this reversed circular polarized light hits again the quarter wave plate, becoming linearly polarized but orthogonal to its original direction and passes the beam splitter unhindered towards the output. To let the two orthogonal polarized beams interfere with each other, an additional polarizer in front of the detector is needed to select out the components of the light that are overlapping. A schematic of the setup is displayed in Fig. 4.4.

- Retro-reflectors for being insensitive to tilt: Any misalignment of the mirrors leads to interference of tilted wavefronts and so a fringe pattern appears on the detector that decreases the captured signal strength. One very common solution to this is the usage of retro-reflectors. They are also called corner cubes as they consist of three mirrors with a  $90^\circ$  angle between them. No matter which angle the incident beam has, they always reflect the beam back into the same direction but slightly translated. Retro-reflectors make alignment much easier because they are not sensitive to tilt but lateral movement could be an issue because the displacement of the out-coming beam is twice the lateral translation of the retro-reflector.

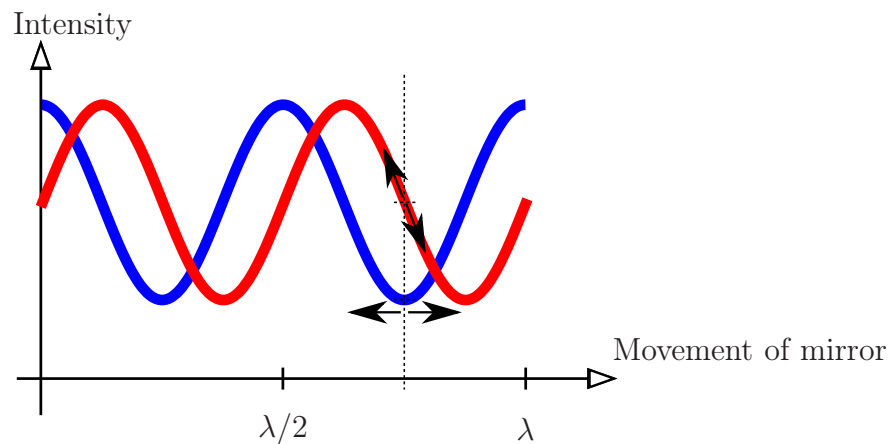


Figure 4.3: The direction of movement can be determined by an additional output with a  $90^\circ$  phase shift. If one output is at an extremum the decrease or increase of the other one shows the direction of movement.

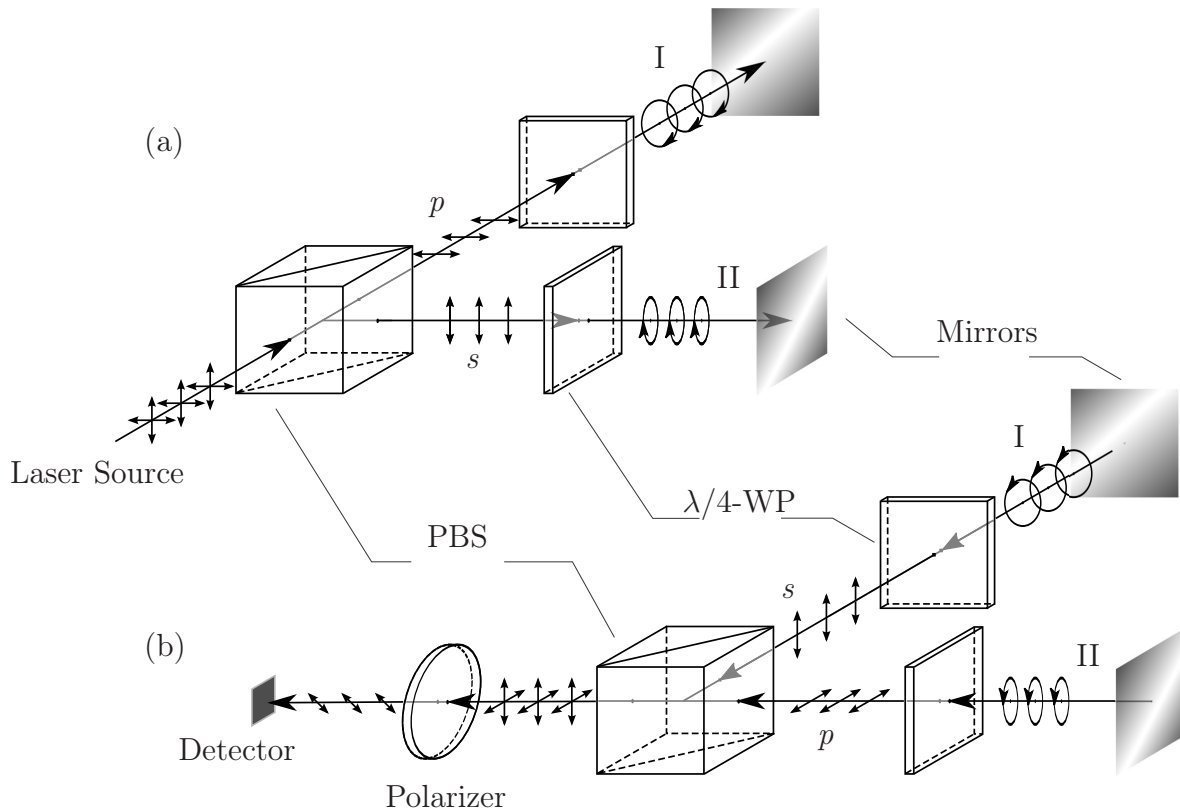


Figure 4.4: In (a) the path from the light source to the reflection on the mirrors is depicted. Orthogonal polarized light hits the PBS where the  $p$  polarization can go through unhindered (path I) while the  $s$  polarization is deflected (path II).  $\lambda/4$ -waveplates transform linear into circular polarized light which then hits the mirrors. In (b) the path after reflecting off the mirrors is displayed. The circular polarization switches direction and the  $\lambda/4$ -waveplates transform the circular polarization back into a linear polarization. The  $s$  polarized light (now from path I) is deflected while the  $p$  polarized light (path II) can go straight through the PBS. The light paths are recombined at the output of the PBS and a polarizer filters out the overlapping components of the two polarizations to enable interference.

### 4.2.2 Disturbances in Interferometric Metrology

The problem of disturbances in the optical measurement path of an interferometer is already covered partly in literature, mainly speaking of the impact of air turbulences and temperature flow of the surrounding atmosphere. In [31] an investigation is conducted on how an air turbulence in a typical distance measuring setup, as can be found in the semiconductor industry, influences the accuracy. Manufacturing processes in the semiconductor industry need very low densities of airborne particle contaminations and therefore use a constant flow of filtered air through the equipment. Together with small thermal gradients this flow of air influences the refraction index based on time-dependent temperature and pressure fluctuation. Measurement errors between 1,6 nm and maximal 24,8 nm were observed, however the author describes that the air disturbance only uncovers if a lot of other error sources, such as vibrations affecting the setup, different refraction indices for the measurement and the reference part (coming from a different mean temperature of the surrounding air) or an uncertain frequency of the used laser are fixed.

The authors in [4] use wavefront measurements of the optical path to model disturbances caused by air turbulences, however don't actively compensate for it. It is described that disturbances move like bubbles through the measurement path and with the help of a multi-segment detector, the disturbance is estimated. This information is fed into a turbulence model which is used to correct the position signal of a waver stage.

A very recently published paper [32] describes the use of an AO system in an interferometric velocity measurement through a fluctuating gas-liquid. By using a fast deformable mirror and a SH sensor with high frame rate they obtain high control bandwidth for low order distortion correction. The results show that an AO system can successfully be integrated in a interferometer (of a Mach-Zehnder style) setup by increasing the contrast of the interference.

### 4.2.3 Conclusion

Incorporating the mentioned improvements, modern interferometers are capable to deliver multi-axis measurement signals with a resolution of 0,31 nm at a data rate of up to 10 MHz.

This thesis aims for a proof of concept if an AO system can enhance the signal strength of the output of a Michelson interferometer. To study the impact of wavefront aberrations on the detector signal of the interferometer a basic Michelson interferometer scheme has been selected since it can be concluded that the AO compensation technique will also work with the improved Michelson interferometers.

### 4.3 Experimental Setup

The proposed setup is drawn in the schematic seen in Fig. 4.5 and combines the adaptive optics system (compare Fig. 3.1) with the Michelson interferometer (compare Fig. 4.2).

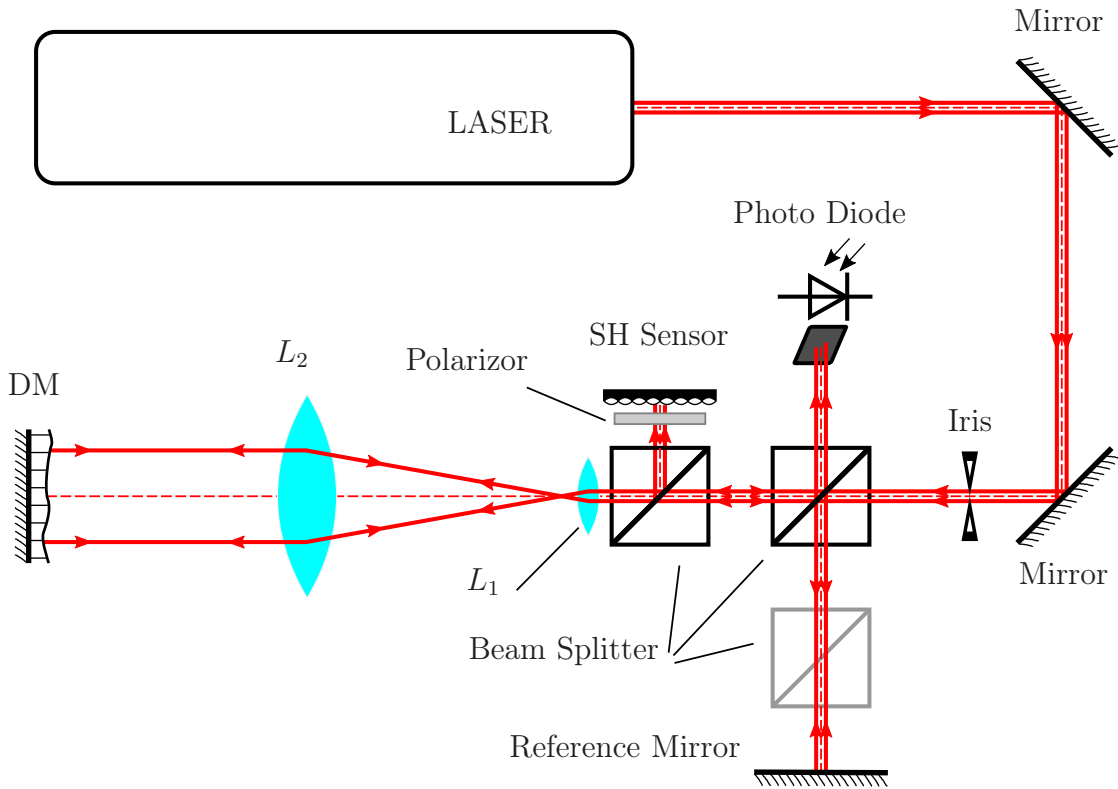


Figure 4.5: Schematic of the actual experimental setup.

The Michelson interferometer is chosen to apply a proof of principle. The basic setup is relatively simple, does not require an excessive amount of components, works with almost any homodyne laser source and a simple photo-diode can be used to record the output signal.

At first, one major difference of the actually build setup to the regular Michelson interferometer is that the measurement mirror is now replaced by the deformable mirror. And additional to that, it is fixed to the optical table and instead the reference mirror sits on a displaceable stage. The main reason for that is that the DM is comparably heavy and bulky and according to the equations of the interferometer's output signal in Eq. (4.8) it is irrelevant which of the two mirrors move. The measured effect comes only from a change of their phase shift and this is achieved by changing the OPL in any of the paths.

The reason why it's still called the measurement path is the introduced aberrations. The aberration disturbs the wavefront of the laser beam and after the interference with the reference path it leads to a non-uniform interference pattern (see also Fig. 1.1).

A change of the OPL of half a wavelength (i.e. quarter of a wavelength displacement of the mirror) results in an inversion of the interference pattern. Illuminated fringes

## 4 Interferometer System

darken and dark ones are now illuminated. The photo detector averages the intensity over its entire sensor area and thus only the change of one fringe is detected. In other words, with a stronger aberration in the measurement path the number of fringes on the detector increases and therefore the change in the output signal (i.e. the signal's peak-to-peak range) is weaker.

To record the signal from the photo detector an I/O device is used, namely the NI USB-6211 from National Instruments<sup>TM1</sup>. It is connected via USB to the PC, all measurements are conducted in MATLAB<sup>®</sup>.

A moveable stage is used to drive the reference mirror continuously. It is an piezo driven device with a minimum step size of 50 nm and together with a controller and an externally provided triangle signal the stage is set to move several micrometers back and forth. This provides a sinusoidal signal at the interferometer's output which then can be used to investigate the influence of different wavefront aberrations on the signal's peak-to-peak range.

The laser produces a beam of approximately  $d_{beam} = 5$  mm in diameter. With the help of two deflection mirrors the beam is adjusted to go perpendicular to the edges of the optical board where the entire system is placed. The first beam splitter that is hit by the beam is the one that creates the interference. There it's divided into the measurement path going to the left and the reference path going downwards. Following along the measurement path the light passes another beam splitter (where only one output is used) and further into a beam expander, consisting of two lenses. These lenses are used to widen the beam to provide a good covering of the surface of the DM which in this setup is used as the measurement mirror. As described in Chapter 3.3, the DM has a diameter of  $d_{DM} = 30$  mm and with the used lenses

- $L_1 : f_1 = 45$  mm and
- $L_2 : f_2 = 180$  mm

the laser beam is expanded four times leading to an illuminated disk of about 20 mm.

The light rays need to go through the beam expander, reflects off the DM and go back through the same two lenses again. This turned out to require a lot of adjustment to get again the same collimated beam as before and the best results were achieved by using so called Air-Spaced Achromatic Doublets from Thorlabs GmbH. Although, only light with a single frequency was used (achromatic lenses are normally designed to cope for chromatic aberrations) they worked best in providing a high-precision focus point in both directions.

Another important thing to take care of is the optical conjugation as described in [24, p. 62]. Even so the light coming to the wavefront sensor is meant to be a collimated beam the sensor should be positioned in a way that the pupil of the optical system is optically conjugated with the pupil of the Shack-Hartmann sensor. Or in other words, the deformable mirror and the Shack-Hartmann sensor have to be placed in the focal/backfocal plane of the lens system to ensure conjugation. If this condition is not adhered, the AO compensation will not work properly.

According to the guideline provided by the manufacturer of the mirror [24], the surface of the DM should not be entirely covered by the beam. From the basic cal-

---

<sup>1</sup>National Instruments Corporation, 11500 Mopac Expwy, Austin, Texas



ulation of the deformation of a plate with biharmonic equations it can be derived that for a proper reconstruction of Zernike modes at least some actuators have to be positioned outside of the used aperture. Or more specific, for a piezo driven mirror like the one used here at least 14 actuators have to act outside of the beam diameter to form Zernike modes of higher order. The particular layout of the mirror as seen in Fig. 3.12b provides this (18 of 19 actuators are outside the used aperture) and in addition to this it's free from any print-through effect.

When the beam reflects off the DM light goes back through both lenses ending up in the same diameter as it started and via the left beam splitter half of it goes to the SH sensor where the wavefront is measured. The microlens array of the SH sensor has a focal length of  $f_{SH} = 7$  mm. In front of the sensor a polarizer is used to weaken the intensity of the incident light. This is necessary to prevent the CCD from overexposure, because the settable range of the exposure time was not sufficient for decent image quality.

The other half of the returning light travels to the next beam splitter. This is the one for the interferometer feature and here it's brought together with the beam from the reference path. As visible in the schematic also a gray beam splitter is drawn in the reference path. Actually, this one has the only use to weaken the intensity of the reference beam the same way the measurement path is weakened by the beam splitter for the wavefront sensor and makes sure that the interfering waves have an amplitude as equal as possible, which is required by Eq. (4.8). The output signal of the interferometer is recorded with the photo diode on top of the interferometer's beam splitter.

### Built Setup

The photo in Fig. 4.6 shows the actual built setup (compare Fig. 4.5) where the path of the laser beam is sketched with a red line. It is set up on a 600 mm  $\times$  900 mm optical breadboard. The picture misses the photo diode that would be placed where the pictograph is as well as the movable stage of the reference mirror (number 4). The description according to the numbers in the picture:

1. *laser source*,  $\lambda = 633$  nm
2. *first beam splitter*, for the Michelson interferometer
3. *beam splitter*, in the reference path for equal intensity in both paths
4. *reference mirror* (not on the photo: movable stage)
5. *beam splitter*, for the wavefront sensor
6. lens  $L_1$ ,  $f_1 = 45$  mm
7. lens  $L_2$ ,  $f_2 = 180$  mm
8. *deformable mirror*
9. *Shack-Hartmann wavefront sensor*

## 4 Interferometer System

10. *iris*, to modify incoming laser diameter
11. *polarizer*, to adapt intensity for the SH sensor

It showed throughout the entire work that the alignment of the setup is the number one crucial condition. Only a small deviation in the optical path destroys the fine tuning of the component's performance.

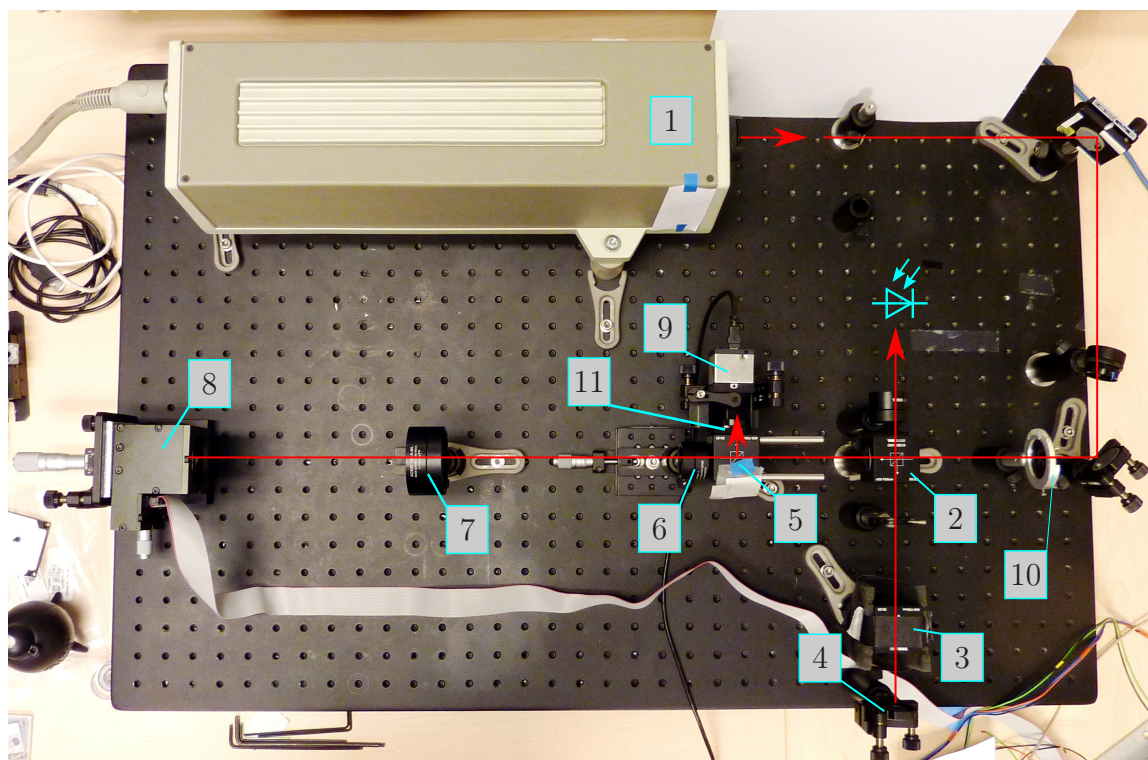


Figure 4.6: Photo of the built setup with a sketched laser path. Not on the photo are the photo diode and the movable stage of the reference mirror.

### 4.4 Results 2: Evaluation of AO in the Interferometric Setup

The main goal of this thesis is to show that an adaptive optics system improves the functionality of a Michelson interferometer setup in a way that if the measurement path suffers from wavefront aberrations the output signal peak-to-peak value range can be increased by counteracting these disturbances. Firstly, an investigation is done on how individual modes, formed by the deformable mirror, are affecting the output signal's peak-to-peak value. And secondly, a test with a variety of arbitrary but static disturbances is conducted and the enhancement through the AO system on the photo detector signal is observed and interpreted.

#### 4.4.1 First Series of Tests: Influence of designated Zernike modes

For this series of tests the mirror is forced to take the shape of one designated Zernike mode at a time. The peak-to-peak value of the output of the Michelson interferometer is recorded to see if and how the induced Zernike mode will result in a loss of signal strength. The procedure for conducting the measurements was as follows:

At first, the gain factor of the designated mode was set to zero while the controller had time to make sure the reflected wave is as even as possible. This plane wave is used as reference in the following. After this the coefficient is increased linearly in ten steps. In every step the controller has time to form the mode sufficiently pure. After every run the interferometer output (i.e. the signal of the photo detector) is measured and the resulting peak-to-peak value is determined. It can be expected that with an increasing coefficient the number of emerging fringes increases on the detector. A movement of one half of a wavelength is still resulting in the change of only one fringe, the share of this one fringe on the whole detector is much smaller compared to a pattern with less fringes. A depiction of this is shown in Fig. 4.7.

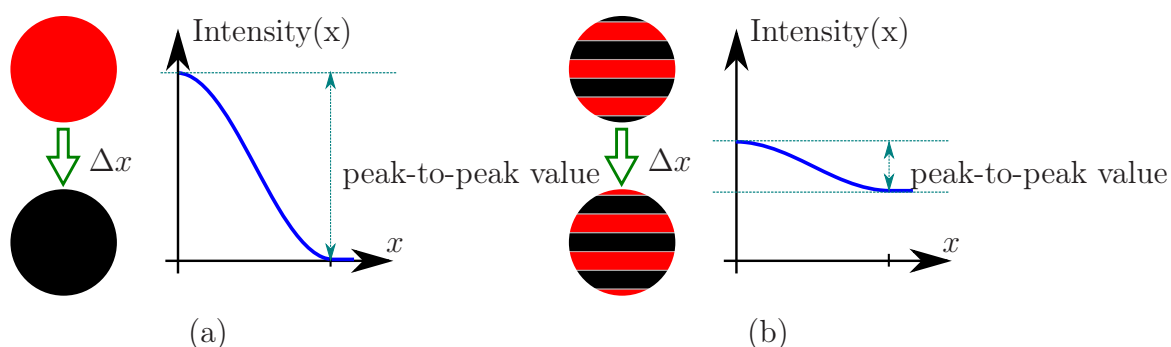


Figure 4.7: In (a) two plane waves interfere. By displacing the mirror by  $\Delta x = \lambda/2$  a drop in intensity from the maximum to zero is noticeable. In (b) a fringe pattern, caused by uneven wavefronts, is visible and if the mirror is moved the same distance only a weaker peak-to-peak value is measurable with the photo-detector.

To make sure the signal on the photo diode is going from the possible minimum to its maximum the mirror of the reference path is moved for more than one wavelength. In a normal interferometer setup the reference is not moved at all but the mirror of the measurement path. Since in this setup the measurement path is terminated by the deformable mirror it seems to be a better choice not to move the comparatively heavy and bulky DM. In a further improved setup the DM would be tilted a little bit to the side, deflecting the beam to an additional mirror. This mirror would be mounted on the moving object. For this particular measurements the moved path itself is not important but a good signal on the photo detector and therefore it is equivalent if the measurement path moves or the reference.

The introduced procedure is now shown for the 3<sup>rd</sup> mode. The target value of the coefficient is increased linearly by  $\Delta c_{z3} = 0,5 \times 10^{-7} \text{ m} = 0,079 \lambda$  for ten times

#### 4 Interferometer System

leading to a final value of  $c_{z3,final} = 5 \times 10^{-7} \text{ m} = 0,79 \lambda$ . This final value was chosen in particular to have comparable results for the first five modes. As it is visible in Fig. 3.22 the DM is able to achieve this coefficient with a high purity (compare Fig. 3.23).

Picking out the third Zernike mode and comparing the output of the interferometer's photo detector at three distinct coefficients (namely,  $c_{z3} = 0$ ;  $1 \times 10^{-7} \text{ m}$  and  $5 \times 10^{-7} \text{ m}$ ) leads to the measured time signals displayed in Figure 4.8. As expected all of them are sinusoidal shaped which comes from a nearly constant movement speed of the mirror. It must be stated that they are not synchronized in any way and the signals are recorded at different times. The important difference between them is the decline of signal strength with an increase of the applied Zernike mode coefficient. The peak-to-peak value is determined as the difference of the maximum and minimum, seen also in Fig. 4.8. Two horizontal light-blue lines for the run where  $c_{z3} = 0$  showing which values are chosen for further processing.

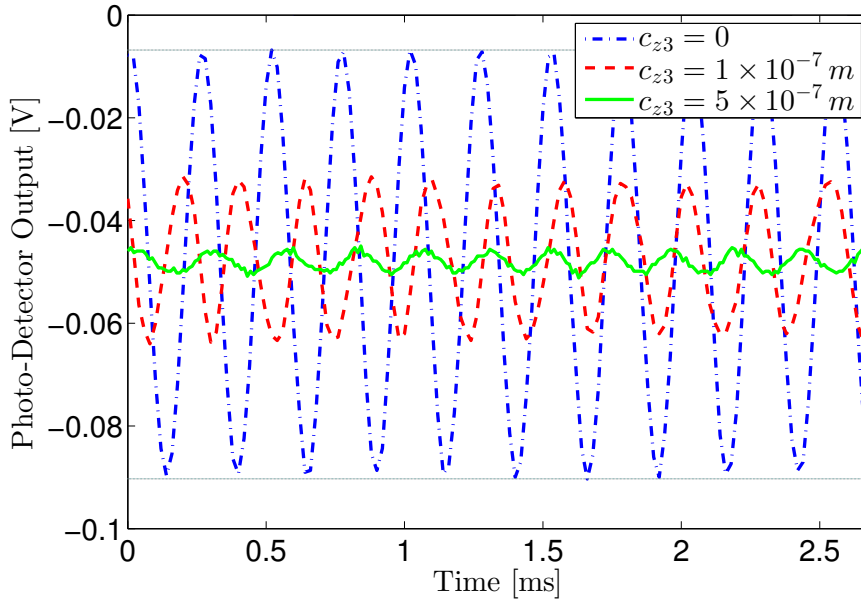


Figure 4.8: Cut-out sequence of the interferometer's output signal showing the influence of a specific wavefront deformation on the output signal when moving the mirror along one direction. Every graph is taken with a different coefficient of the third Zernike mode. The disturbance is varied from weak ( $c_{z3} = 0$ ) to heavy ( $c_{z3} = 5 \times 10^{-7}$ ).

Each period in the detector signal represents a displacement of the moving mirror of half a wavelength, ergo 316,5 nm. Collecting the acquired peak-to-peak values from every rerun results in Fig. 4.9 where the x-axis describes the increase of the coefficient  $c_{z3,n+1} = c_{z3,n} + \Delta c_{z3}$  and the y-axis describes the measured peak-to-peak signal. The graph shows a definite drop of signal strength with increasing Zernike coefficient.

Fig. 4.10 shows the drop of the interferometer output signal when increasing the coefficients of the first five Zernike modes.

The graph shows one color for each mode and all lines show the tendency to sink

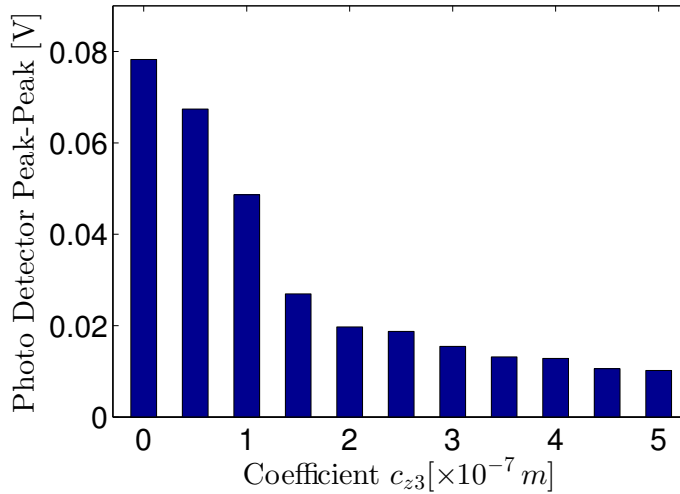


Figure 4.9: Comparison of the measured peak-to-peak value of the photo detector signal with increasing coefficient  $c_{z3}$  of Zernike mode number 3.

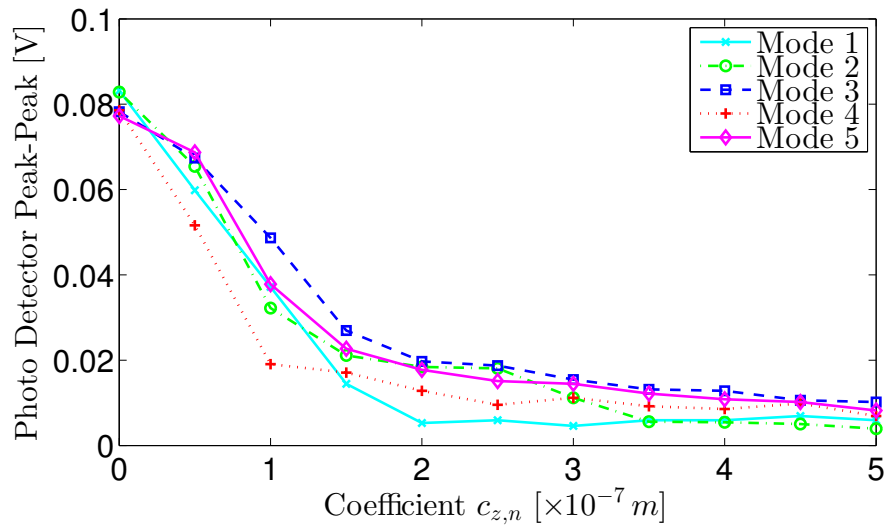


Figure 4.10: Peak-to-valley signal of the detector output when increasing the gain factor  $c_{zn}$  of the dedicated mode. The first five Zernike modes are used as disturbance source.

with increasing gain factor but with notable differences. For example the similarity between the third and the fifth mode ( $\square$  blue,  $\diamond$  pink) as they are very similar in their behavior, especially if they are compared to the defocus mode (number 4,  $+$  red). This comes mainly from the fact that by applying defocus the entire surface is bended while with astigmatism (mode 3 and 5, compare also Fig. 2.5) mainly the edges are formed and two orthogonal “bridges” remain stable on the surface.

#### 4.4.2 Second Series of Tests: Disturbance Compensation

After investigating the influence of distinct Zernike modes on the interferometer's output signal strength in the previous section, now various disturbances are introduced into the measurement path. The impacts before and after active compensation are measured and presented. Since disturbances can be seen as a superposition of Zernike modes with varying coefficients the aberrations are decomposed into their components and so a connection with the previous measurements is filtered out.

As disturbance source a disc of PMMA was used. The plate is melted slightly in some places with a hot air blower to increase surface irregularities. For the following measurements the disk is fixed in a holder and the laser is going through a small part of the face. Additionally, the disc can be rotated to switch to another disturbance profile.

In the Appendix 2 a compilation of the ten utilized disturbances is shown. All are displayed as interferogram, 3D representation and as Zernike decomposition with the according coefficients. It can be seen that the coefficients are decreasing with higher modes throughout all disturbances and especially after the fifth mode a significant drop is visible. This fact was observable with all investigated disturbances and meets the capability of the AO system which has its strengths in forming lower modes considerably better than higher. The RMS and P-V values for the used ten disturbances are depicted in Fig. 4.11. It was on purpose to have a variety of RMS values (and P-V values, respectively) to test the performance of the system for different circumstances.

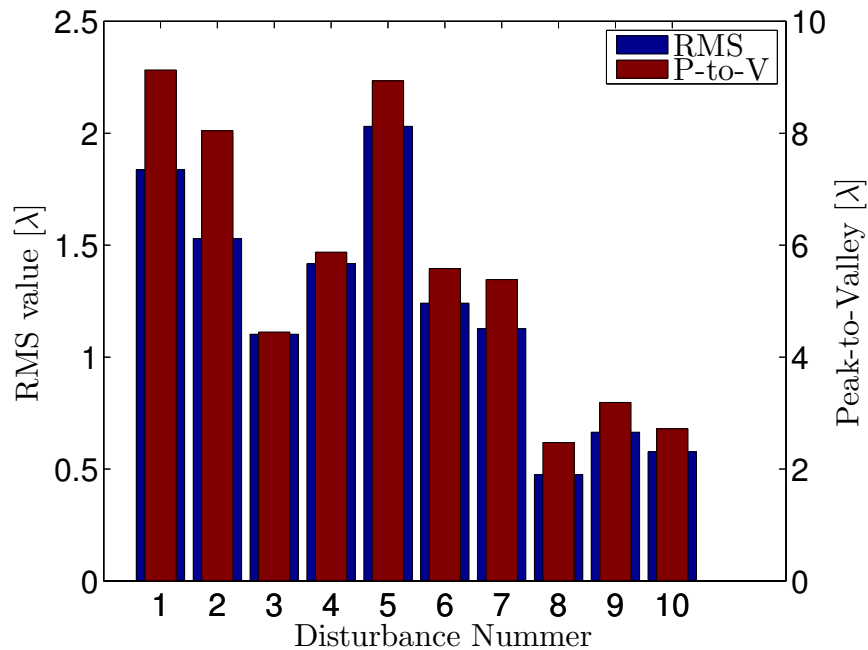


Figure 4.11: Compilation of the RMS value (dark blue) and the P-V value (dark red) of the ten applied disturbances.

The following measurements are carried out to determine on one hand the loss of signal strength on the photo detector caused by the disturbance and on the other hand to show that the signal can be increased by using anAO system. As preferences

#### 4.4 Results 2: Evaluation of AO in the Interferometric Setup

are used the regularization parameter  $\beta = 0,0015$  and a number of 800 cycles for the feedback algorithm to be sure a constant output is established. The experiment was carried out in the following steps:

- no disturbance is applied
- measuring the interferometer's output peak-to-peak value,  $A_0$
- introducing an aberration
- measuring the output again, a smaller peak-to-peak value is expected,  $A_n$
- the feedback controller tries to compensates for the aberration
- again measuring the interferometers output,  $A_{n_{comp}}$ .

The procedure above was repeated for the ten described disturbances in the following labeled as P1 to P10.

To show an example on how the measurement is carried out the disturbance number P5 with two strong tilts is picked out (see representation in Appendix 2). First, the undisturbed signal is acquired leading to an value for the undisturbed peak-to-peak value  $A_0 = 21,0 \text{ mV}$ .

Now the disturbance is introduced by placing the PMMA disk into the laser beam. The signal decreases from  $A_0 = 21,0 \text{ mV}$  to  $A_5 = 4,6 \text{ mV}$ .

When the feedback controller is switched on and the RMS value of the captured wave is monitored a quick drop at the beginning, followed by an asymptotic-like behavior is observed similar to the investigation in Chapter 3.5.1. The residual  $RMS_{residual} = 0,0479 \lambda$  is about two orders of magnitude smaller than the initial value  $RMS_{start} = 2,1460 \lambda$ .

If the amplitude is now determined a third time, in fact after the feedback controller did the work, the obtained value is  $A_{5_{comp}} = 56,5 \text{ mV}$  which is even higher than the originally undisturbed value. That is the case because at the first measurement no active compensation was applied, thus also any system introduced aberrations like imperfect lenses or small misalignment were also effecting the output. While the controller takes care to compensate for the introduced aberrations it also cancels out most of these system immanent errors. Comparing the amplitudes directly

$$\frac{A_{5_{comp}}}{A_5} = \frac{56,5 \text{ mV}}{4,6 \text{ mV}} = 12,2826... \quad (4.17)$$

shows an increase of more than one decimal power.

Putting together the results from the ten conducted tests shows a clear improvement of the signal peak-to-peak value. The amount of improvement depends on the disturbance. The bar graph in Fig. 4.12 shows the comparison of the captured peak-to-peak values against the disturbed ones in blue and the ones with active compensation in green.

The resulting RMS values are displayed in Fig. 4.13 where they can be compared to the starting values in Fig. 4.11. The different scaling of the y-axis in both graphs must be taken into account. The resulting RMS values are about two orders of magnitude

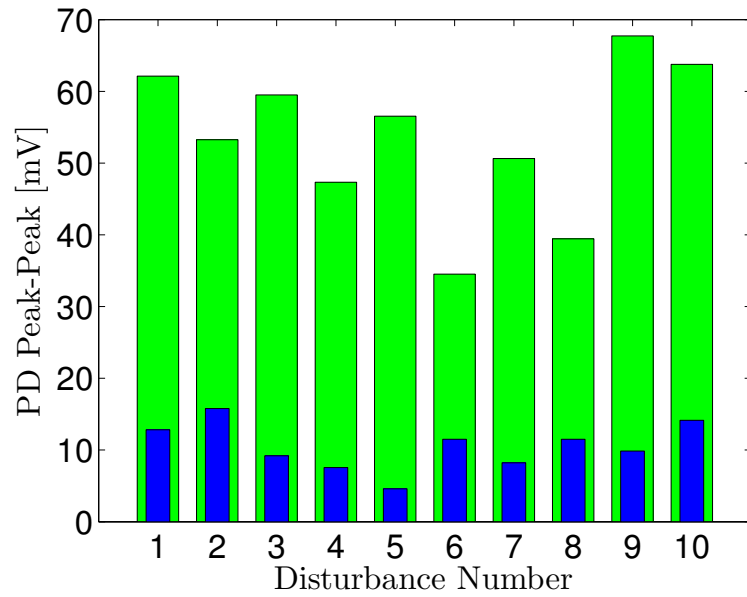


Figure 4.12: Depiction of the captured peak-to-peak values suffering from different disturbances before (blue) and after (green) the feedback controller is activated

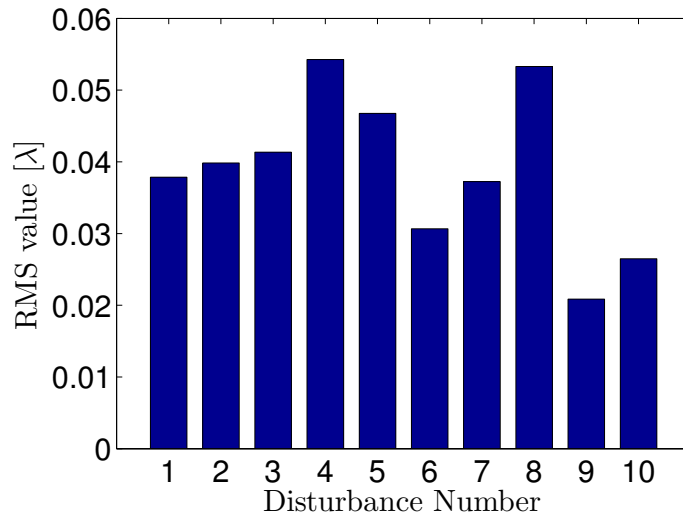


Figure 4.13: Compilation of the RMS values of the resulting wavefronts after the active compensation of the disturbances.

smaller and for the purpose of noise cancellation the presented values are the mean of the last 80 measured data points.

Tab. 4.1 sums up the results for all disturbances and shows the improvement as a factor of compensated to disturbed peak-to-peak value.

In the recorded tests the minimum of the achieved improvement factor is at the sixth disturbance  $A_{6_{comp}}/A_6 = 3,00$  and the maximum at the fifth  $A_{5_{comp}}/A_5 = 12,29$  with an average over all ten values at about 5,72.



Table 4.1: Comparison of AO enhanced interferometer output signals.

Distur. n#	$A_{n_{comp}}$ [mV]	$A_n$ [mV]	$\frac{A_{n_{comp}}}{A_n}$	$RMS_{comp}$ [ $\lambda$ ]	$RMS_n$ [ $\lambda$ ]
P1	62,13	12,82	4,8462	0,0379	1,8376
P2	53,26	15,78	3,3750	0,0399	1,5292
P3	59,50	9,20	6,4643	0,0413	1,1020
P4	47,34	7,56	6,2609	0,0543	1,4169
P5	56,54	4,60	12,2857	0,0468	2,0313
P6	34,52	11,51	3,0000	0,0307	1,2412
P7	50,63	8,22	6,1600	0,0372	1,1271
P8	39,45	11,51	3,4286	0,0533	0,4748
P9	67,72	9,86	6,8667	0,0209	0,6644
P10	63,78	14,14	4,5116	0,0265	0,5769

An explanation why some disturbances are more likely to be compensated than other can be found in their Zernike coefficients. The highest gain in peak-to-peak values was achieved with the disturbance P5 mainly because of its strong first and second coefficient leading to a small initial value  $A_5$ . But since tip and tilt can be formed very efficiently by the mirror the win in signal strength is the highest. Disturbance P6 for example suffers also from a strong tip and tilt together with a relatively strong defocus. Even so the RMS value is one of the smallest this combination demands a very high control variable that drives the actuators into saturation. And particularly disturbance P8 shows a comparable high 14<sup>th</sup> mode which can hardly be formed by the mirror, therefore also a saturation of the actuators and so a worse increase of signal strength.

## 4.5 Conclusion

As conclusion can be said that the proposed setup is capable to improve the output signal's peak-to-peak value of a Michelson interferometer if the laser beam in the measurement path is suffering from wavefront aberrations. In this setup the average increase of the peak-to-valley signal range was 5,4 times the disturbed signal. The amount of improvement depends on the composition of Zernike modes of the disturbances. While even strong tip and tilt compensation is very easily done, disturbances with significant coefficients higher than the 10<sup>th</sup> mode are hard to compensate with the used deformable mirror.

Assuming the photo detector is already working on its detection limit because of a weak laser beam, limit of the resolution of the ADC, noise or even because of working in an environment with strong ambient light, an increase of this magnitude could help establishing an operative interferometer setup even in harsh conditions.



The results from the previous chapter show that the usage of adaptive optics in a Michelson interferometer setup can enhance the output signal's peak-to-peak value. In the following, some issues are presented to support further improvements of the overall system.

For the AO part of the system separate investigations are conducted. The limitations of the SH sensor not to be able to detect the *piston mode* in a wavefront makes the presented setup vulnerable to induced errors due to the movement of the DM itself. If all actuators of the DM are translated uniformly with the same offset no change in the reconstructed wavefront is noticeable but the output of the Michelson interferometer would see a distance change. To prevent this, either the position of the actuators could be recorded together with the wavefront or the mean position of the mirror's surface must be measured with an additional sensor. The first method is limited because of the strong hysteresis of piezo stacks which demands a powerful model to deal with this nonlinearity if only the control signal is used to predict the piston mode. The second method could lead to a massive overhead of extra components. Possible ideas for this piston mode detection are for example an eddy-current sensor or even an additional interferometer that logs the mean position of the mirror.

In this thesis the only regarded disturbance was introduced by a partly melted PMMA disk in a static arrangement. For a further system evaluation a *dynamic approach* is needed, potentially composed of a (hot) airflow together with a nozzle and shielding to make sure only the measurement path is exposed. In general, a next step would need to consider a dynamic disturbance source which results in higher requirements for the speed of the feedback loop. A faster SH sensor together with an optimized algorithm in MATLAB<sup>®</sup> or even an embedded solution (for example in a FPGA) could increase controller speed.

As the results show the strongest modes of the investigated disturbances are mainly tip and tilt. For some cases maybe a mirror with only *tip and tilt correction* would also lead to similar results with the benefit of a simplified control that also would lead to a higher controller speed. This is also thinkable with a simpler wavefront sensor than the

## 5 Outlook

SH sensor where it's not necessary to process an entire image to derive the wavefront.

The other direction to improve the performance of the system would be to implement an AO setup that is able to compensate for even higher modes with sufficient coefficients. As outlined in the Results in Chapter 4.4 the current system is only able to form Zernike modes up to the 15<sup>th</sup> with a positive purity. A DM with a higher number of actuators would be able to correct more Zernike modes but also would need a more powerful driving hardware.

The built interferometer setup is the basic Michelson interferometer and so a way to improve the system's performance would be to implement the enhancements described in Chapter 4.2.1, where possible *Improvements for High-Precision Distance Measurements* are outlined. The utilization of the detection of the moving direction, the usage of a polarizing beam splitter (together with a qualified laser and quarter wave plates) to reduce intensity loss and corner cubes instead of normal mirrors should cause no noteworthy problems for the other features of the system.

Another big step in enhancement that's worth a deeper investigation is given by the introduction of the *heterodyne interferometer*. It is widely used in the interferometric metrology. This setup uses a laser which is capable of sending out two orthogonal polarized beams with a small difference in their frequency (small, compared to the frequency of light). Interference of these two beams leads to a beat signal with the frequency difference as the envelop. The distance measurement is now accomplished by comparing two AC signals as one is tapped right at the output at the laser source and one at the output of the Michelson interferometer. Due to the Doppler-Shift of a moving object in the measurement path the envelop frequency of the second signal is modulated while the first signal is still at the same frequency. Thus, the distance information can be derived from the variation of an AC signal rather than using intensity information. This comes with the advantage of not being sensitive to any loss of laser intensity (as long as the signal is still detectable). Additionally, the direction of movement is directly derived from the Doppler-Shift and also any drift of the laser frequency would not lead to any erroneous measurement as long as both frequencies are drifting equally. This is true in most cases since drift mainly originates from temperature change of the environment. The complete calculation for signal acquisition is done in [29]. An integration of an AO system into a heterodyne interferometer setup could also bring advantages if the wavefront is distorted that much that a proper interference signal can not be read out.

---

## Bibliography

---

- [1] R. K. Tyson, *Principles of Adaptive Optics*, 3rd ed., ser. Series in Optics and Optoelectronics. CRC Press, 2011.
- [2] J. Porter, H. Queener, J. Lin, K. Thorn, and A. Awwal, *Adaptive Optics for Vision Science: Principles, Practices, Design, and Applications*, 1st ed., ser. Wiley Series in Microwave and Optical Engineering. John Wiley & Sons, 2006.
- [3] Z. Li, D. Xiuhua, and C.-H. Wen, “Research on satellite-to-ground optical communication and AO technique,” *International Symposium on Microwave, Antenna, Propagation and EMC Technologies for Wireless Communications*, pp. 794–798, Aug 2007.
- [4] E. Johnstone and D. Y. Abramovitch, “Quintessential phase: A method of mitigating turbulence effects in interferometer measurements of precision motion,” *American Control Conference (ACC)*, pp. 3723–3728, June 2013.
- [5] A. Prechtl, “Elektrodynamik, Skriptum zur Vorlesung,” Institut für Grundlagen und Theorie der Elektrotechnik, TU Wien, 2005.
- [6] J. M. Geary, *Introduction to Wavefront Sensors*, ser. Tutorial Texts Series. Bellingham, Washington: SPIE Press, 1995.
- [7] R. M. Schmidt, G. Schitter, and J. van Eijk, *The Design of High Performance Mechatronics*, 1st ed. Delft: Delft University Press, 2011.
- [8] M. Born and E. Wolf, *Principles of Optics*, 4th ed. Oxford: Pergamon Press, 1970.
- [9] G.-M. Dai, *Wavefront Optics for Vision Correction*, 1st ed. Bellingham, Washington: SPIE, 2008.
- [10] S. Bonora and L. Poletto, “Push-pull membrane mirrors for adaptive optics,” *Optics Express*, vol. 14, no. 25, pp. 11 935–11 944, Dec 2006.

## Bibliography

- [11] K. J. G. Hinnen, “Data-driven optimal control for adaptive optics,” Ph.D. dissertation, Delft University, 2007.
- [12] F. Roddier, *Adaptive Optics in Astronomy*, 1st ed. Cambridge: Cambridge University Press, 1999.
- [13] A. Tozzi, P. Stefanini, E. Pinna, and S. Esposito, “The double pyramid wavefront sensor for LBT,” *SPIE Proceedings*, vol. 7015, pp. 701 558–701 567, July 2008.
- [14] A. Burvall, E. Daly, S. R. Chamot, and C. Dainty, “Linearity of the pyramid wavefront sensor,” *Optics Express*, vol. 14, no. 25, pp. 11 925–11 934, Dec 2006.
- [15] R. Gilmozzi, “Science, technology and detectors for extremely large telescopes,” *Experimental Astronomy*, vol. 19, no. 1-3, pp. 5–13, January 2005.
- [16] N. Doble and D. R. Williams, “The Application of MEMS Technology for Adaptive Optics in Vision Science,” *IEEE Journal of Selected Topics in Quantum Electronics*, vol. 10, no. 3, pp. 629–635, May 2004.
- [17] R. H. Freeman and J. E. Pearson, “Deformable mirrors for all seasons and reasons,” *Applied Optics*, vol. 21, no. 4, pp. 580–588, Feb 1982.
- [18] R. P. Grosso and M. Yellin, “The membrane mirror as an adaptive optical element,” *Journal of the Optical Society of America, (JOSA)*, vol. 67, no. 3, pp. 399–406, Mar 1977.
- [19] E. Dalimier and C. Dainty, “Comparative analysis of deformable mirrors for ocular adaptive optics,” *Optics Express*, vol. 13, no. 11, pp. 4275–4285, May 2005.
- [20] S. Thomas, T. Fusco, A. Tokovinin, M. Nicolle, V. Michau, and G. Rousset, “Comparison of centroid computation algorithms in a Shack-Hartmann sensor,” *Monthly Notices of the Royal Astronomical Society*, vol. 371, no. 1, pp. 323–336, July 2006.
- [21] M. Thier, R. Paris, T. Thurner, and G. Schitter, “Low-Latency Shack-Hartmann Wavefront Sensor Based on an Industrial Smart Camera,” *IEEE Transactions on Instrumentation and Measurement*, vol. 62, no. 5, pp. 1241–1249, May 2013.
- [22] M. E. Wall, A. Rechtsteiner, and L. M. Rocha, “Singular Value Decomposition and Principal Component Analysis,” *ArXiv Physics e-prints/0208101*, pp. 91–109, Aug 2002.
- [23] OKO Technologies, *19 - channel piezoelectric deformable mirror system, technical passport*, Flexible Optical B.V., Rijswijk, The Netherlands, 2011.
- [24] OKO Technologies, *Adaptive Optics Guide*, 3rd ed., Flexible Optical B.V., Rijswijk, The Netherlands, April 2008.
- [25] G. Bertotti and I. D. Mayergoyz, *The Science of Hysteresis*, 1st ed. Academic Press, 2006.

- [26] C. Paterson, I. Munro, and J. Dainty, “A low cost adaptive optics system using a membrane mirror,” *Optics Express*, vol. 6, no. 9, pp. 175–185, Apr 2000.
- [27] A. Polo, A. Haber, S. F. Pereira, M. Verhaegen, and H. P. Urbach, “An innovative and efficient method to control the shape of push-pull membrane deformable mirror,” *Optics Express*, vol. 20, no. 25, pp. 27 922–27 932, Dec 2012.
- [28] P. C. Hansen, “The L-curve and its use in the numerical treatment of inverse problems,” *Computational Inverse Problems in Electrocardiology*, ed. P. Johnston, *Advances in Computational Bioengineering*, pp. 119–142, 2000.
- [29] R. Loughridge and D. Abramovitch, “A tutorial on laser interferometry for precision measurements,” *American Control Conference (ACC)*, pp. 3686–3703, June 2013.
- [30] H. Butler, “Position Control in Lithographic Equipment,” *IEEE Control Systems Magazine*, vol. 31, no. 5, pp. 28–47, Oct 2011.
- [31] N. Bobroff, “Residual errors in laser interferometry from air turbulence and non-linearity,” *Applied Optics*, vol. 26, no. 13, pp. 2676–2682, Jul 1987.
- [32] L. Büttner, C. Leithold, and J. Czarske, “Interferometric velocity measurements through a fluctuating gas-liquid interface employing adaptive optics,” *Optics Express*, vol. 21, no. 25, pp. 30 653–30 663, Dec 2013.





### 1 Disturbances for Control Gain Finding

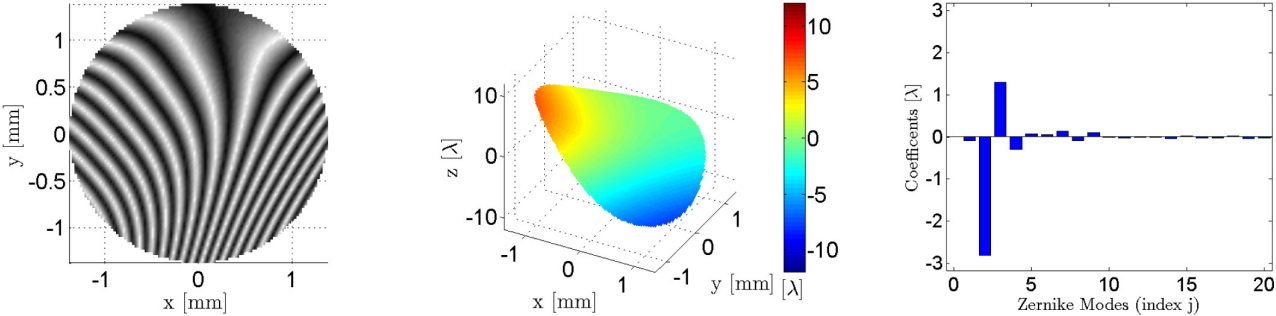


Figure 1: Disturbance G1

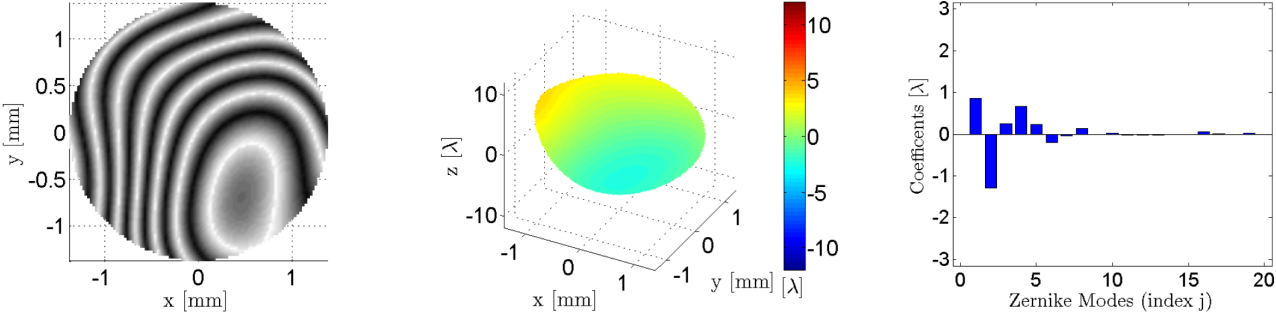


Figure 2: Disturbance G2

Appendix A: Measurement Display

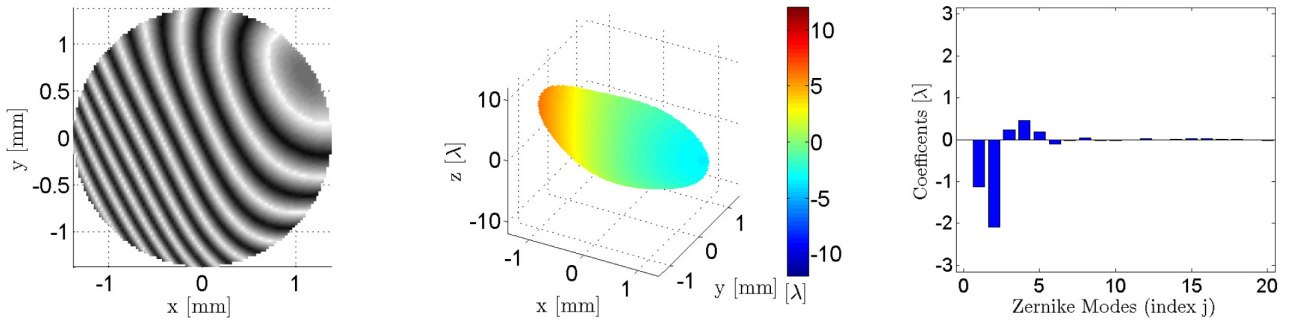


Figure 3: Disturbance G3

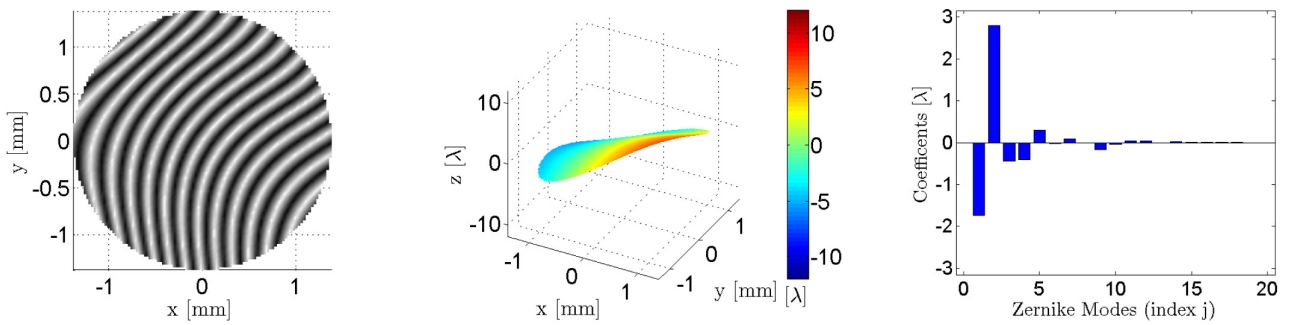


Figure 4: Disturbance G4

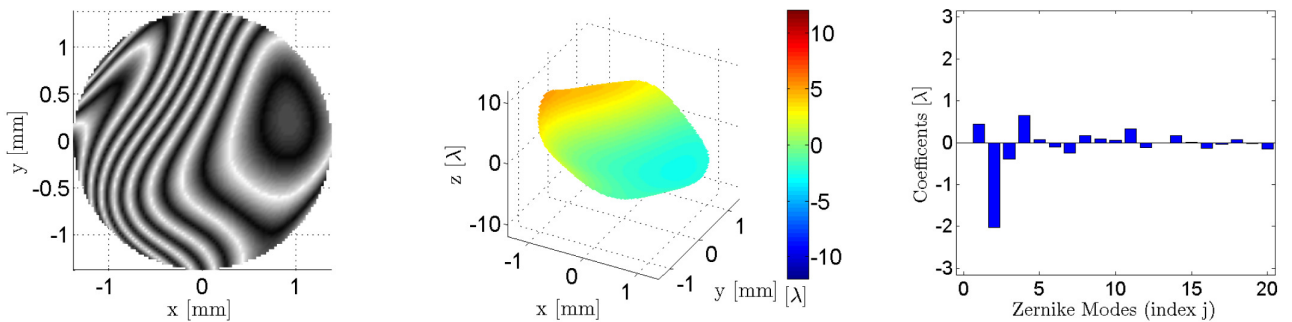


Figure 5: Disturbance G5

## 2 Disturbances for Performance Testing

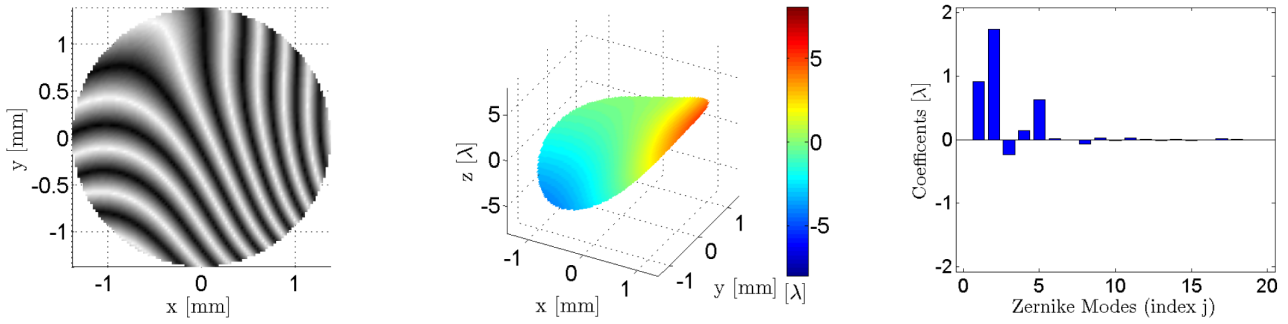


Figure 6: Disturbance P1

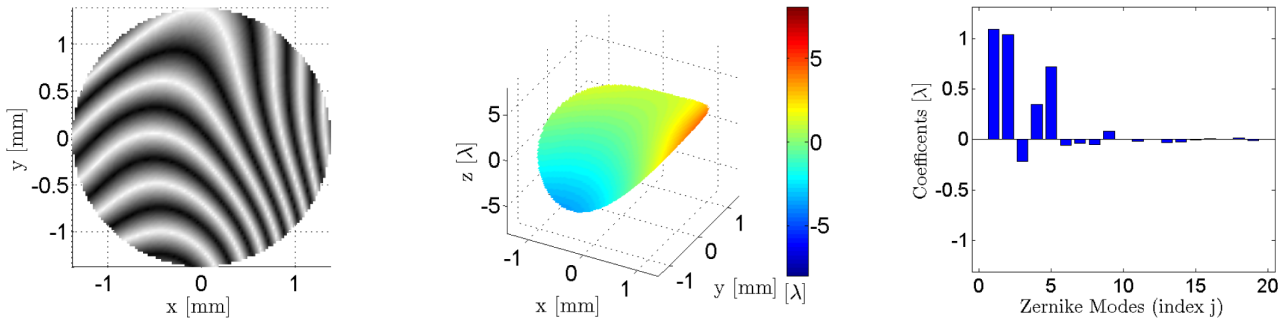


Figure 7: Disturbance P2

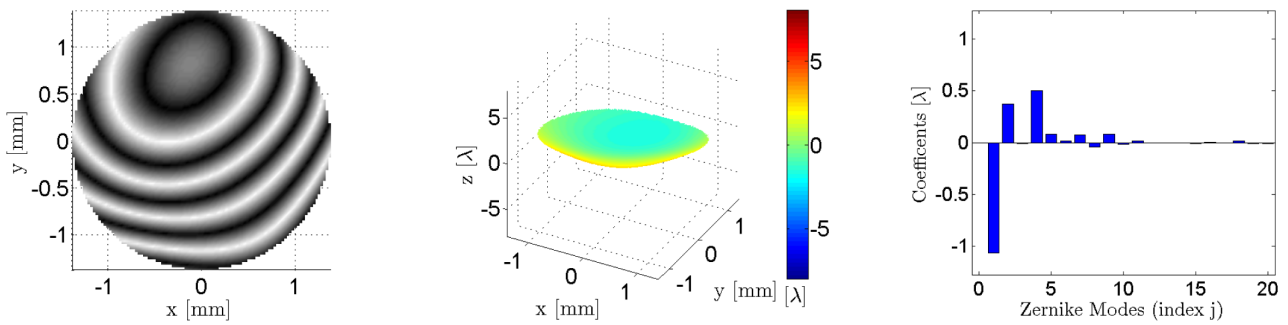


Figure 8: Disturbance P3

Appendix A: Measurement Display

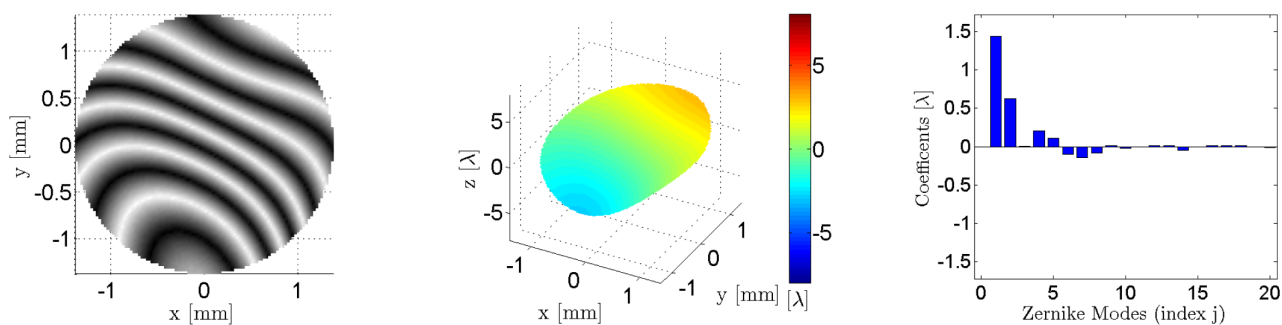


Figure 9: Disturbance P4

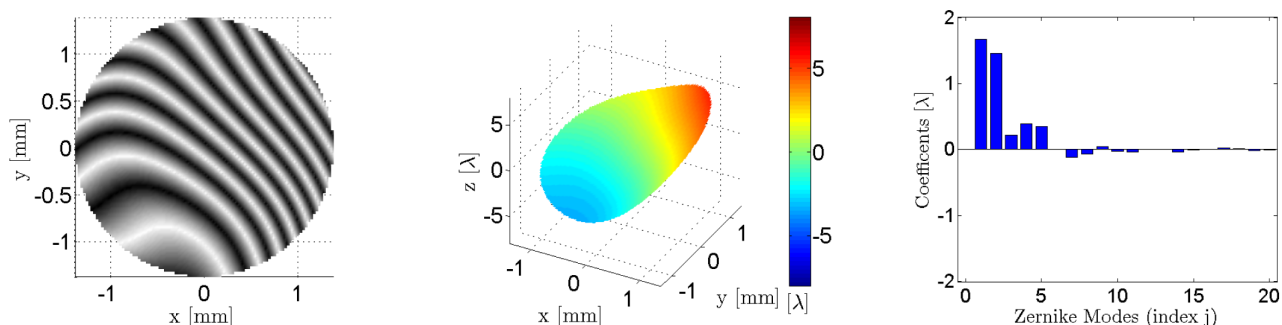


Figure 10: Disturbance P5

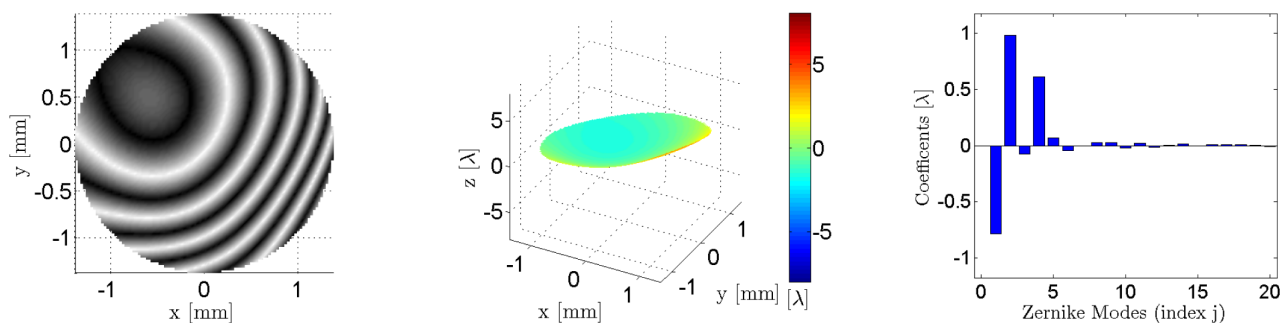


Figure 11: Disturbance P6

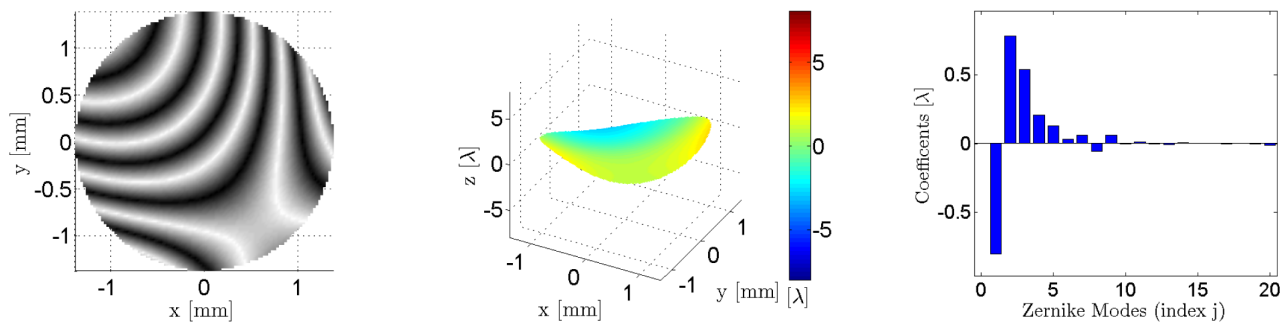


Figure 12: Disturbance P7

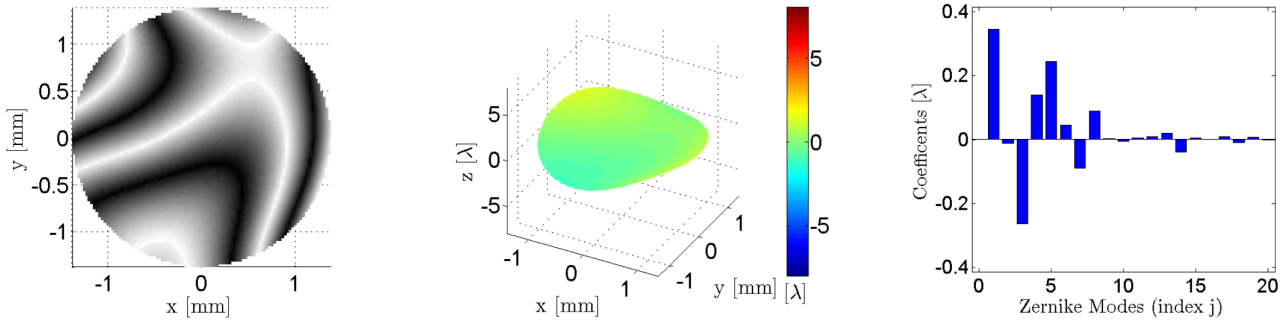


Figure 13: Disturbance P8

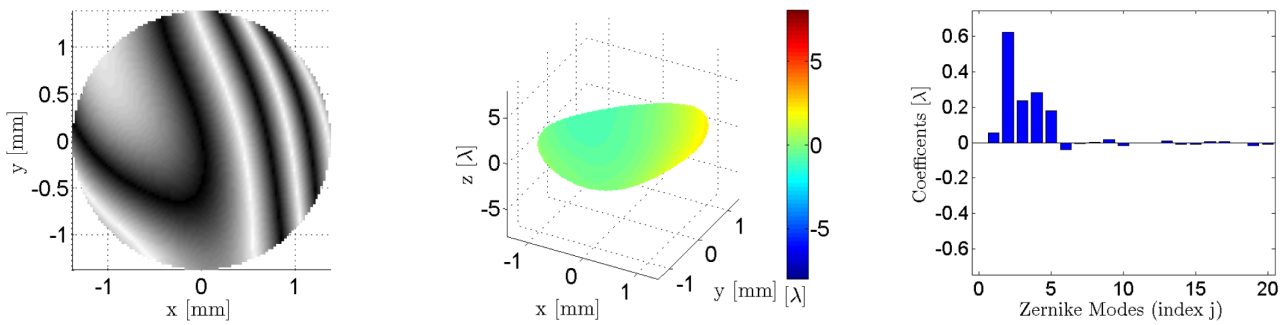


Figure 14: Disturbance P9

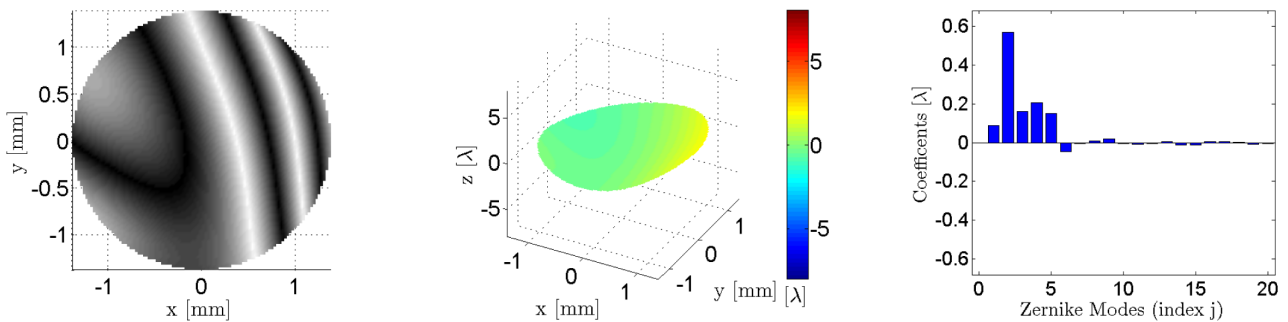


Figure 15: Disturbance P10



### 3 Driving the Deformable Mirror

To drive the DM a high voltage driver for the piezo stacks is needed together with a DAC that receives the control signals from the PC. The DAC is connected via an Ethernet connection to the PC while flat ribbon cables connect the driver and the mirror.

One point that must be stated is that the mapping of the physical connector to the actuator number does not match the description in the manual. A conversion from the connector indices to the ones from the actuators was identified by applying voltage to each piezo stack individually and determining its position by evaluating the corresponding wavefront captured with the SH sensor. In Table 1 the mapping is shown and if for example the first actuator (i.e. the center stack) is addressed the index is mapped to pin 8 of the connector, according to the conversion table.

Table 1: Mapping of the indices of the actuators to the physical connector.

actuator	connector	actuator	connector
1	8	11	18
2	19	12	11
3	13	13	15
4	17	14	16
5	14	15	4
6	6	16	5
7	2	17	9
8	7	18	3
9	1	19	10
10	12		





---

## Appendix C: Software Functions

---

```
[time, data] = NI_USB_6211_Analog_Measurement(nbr_points, time_s);
```

Delivers the output of the National Instruments<sup>™</sup> ADC. Inputs are the number of points and the duration time that should be recorded in seconds.

```
[hpreview, uEye_obj] = init_imaqtool_settings(exp, prev, grid);
```

Initialization of the MATLAB<sup>®</sup> image acquisition toolbox settings. The exposure is set with `exp`. If `prev` is non zero, a live preview is enabled, optional with `grid` on (non zero) or off (zero).

```
ref = reference_measurement(snapshot, handle,...  
    ... tresh_low, tresh_high, sub_size, nbr_lenses);
```

Provides the reference centroids for the SH sensor as return value as well as saving them as 'Reference\_Centroids.mat'. Inputs are an undisturbed SH `snapshot`, a `handle` to the preview object to plot the reference centroids, a `threshold _high` and `_low` where the pixel intensity is limited, the size of the subaperture in pixels `sub_size` and the number of utilized lenses.

```
colmap = colormap_interference_generator(stripes);
```

This functions constructs a colormap to display interference fringes. With the input `stripes` the visible fringes are set. The borders of the graph where this colormap is used need to be adjusted manually to the number of fringes and the used wavelength.

```
socket = DAC_init_and_open();
```

Initialization routine for the DAC that drives the piezo actuators of DM. An Ethernet connection is established and a `socket` number is returned which must be used whenever the DAC is addressed.

```
DAC_close(socket);
```

Closes the Ethernet connection to the socket assigned by the previous function.

## Appendix C: Software Functions

```
Send_values_to_DAC(socket, int32(v_desire));
```

A voltage vector `v_desire` is sent to the DM's actuators, addressed by the opened Ethernet `socket`. The input format for the voltage array must be an array of 32-bit integer values.

```
slopes = slopes_calculation(snapshot, ref, nbr_lenses, pxl_size, focus);
```

Calculates the slopes  $s_x, s_y$  out of a SH `snapshot`. Further inputs are the reference centroids (`ref`), the number of utilized lenses (`nbr_lenses`), the size of one single pixel (`pxl_size`) and the focus of the lenses.

```
[phi, coeff_Z] = wavefront_calculation(snapshot, ref, nbr_lenses, ...  
... pxl_size, focus, diam);
```

Calculates the 3D wavefront and the according Zernike coefficients out of a SH `snapshot`. Further inputs are the reference centroids (`ref`), the number of utilized lenses (`nbr_lenses`), the size of one single pixel (`pxl_size`), the focus of the lenses and the diameter of the sensor (`diam`).